

1 **A hybrid physics–ML framework for integrating groundwater**
2 **dynamics into land surface modeling**

3 **Chen Yang^{1*}, Hui Huang¹, Zeyu Tang¹, Yongjiu Dai¹, Xiaobin Chang²**

4 ¹School of Atmospheric Sciences, Sun Yat-sen University, Zhuhai, China

5 ²School of Artificial Intelligence, Sun Yat-sen University, Zhuhai, China

6
7 **Corresponding to: yangch329@mail.sysu.edu.cn**

17 **Abstract**

18 Three-dimensional groundwater dynamics play a critical role in regulating land-
19 atmosphere interactions, yet resolving three-dimensional subsurface flow processes at large
20 scales remains computationally prohibitive. Here we present a hybrid coupling framework
21 that enables the integration of three-dimensional groundwater processes into land surface
22 modeling at substantially reduced computational cost. The framework replaces the physics-
23 based groundwater solver with a deep learning surrogate while preserving the original
24 coupling interface, providing a practical pathway for incorporating groundwater dynamics
25 into Earth system simulations. A key feature of the framework is an error-control strategy
26 based on a free-drainage lower bound, which approximates the treatment of subsurface
27 processes in conventional land surface models where groundwater feedback is largely
28 neglected. The hybrid solution is considered acceptable as long as its deviation remains
29 within this free-drainage bound, with a user-defined threshold providing additional control
30 over acceptable error levels, enabling flexible, application-dependent control of model
31 fidelity. The framework is demonstrated in a $\sim 34,000$ km² watershed in the Pearl River Basin,
32 China, achieving an approximately 20 \times speedup while maintaining strong agreement with
33 the physics-based reference. Over a full-year hourly simulation, the median water table depth
34 error is within 0.5 m and the domain-averaged latent heat flux reaches a Kling-Gupta
35 efficiency of 0.965. This study demonstrates the feasibility of hybrid surrogate-
36 physics coupling for representing groundwater processes and provides a flexible foundation for
37 multi-timescale, on-demand simulations, with potential for extension to diverse
38 hydroclimatic settings and integration into Earth system modeling frameworks.

39 **1. Introduction**

40 Machine learning (ML) is increasingly transforming the geosciences, driving Earth
41 system models to evolve from purely physics-based frameworks toward hybrid physics-ML
42 architectures. Several forms of hybridization have emerged, each serving distinct objectives
43 (Chen et al., 2023).

44 In cascade mode, physical and ML models are executed sequentially, with the output of
45 one serving as the input of the other. For example, meteorological drivers can be downscaled
46 using ML for land surface simulations—acting as post-processing relative to climate models
47 and as pre-processing relative to land models (Chen et al., 2024). In addition to such
48 applications, dedicated datasets have also been developed to facilitate this hybridization.
49 The ClimSim dataset (Yu et al., 2023), generated from high-resolution E3SM simulations, has
50 enabled the efficient development of ML emulators for computationally expensive subgrid
51 processes, allowing ML researchers to contribute without directly handling domain-specific
52 physical models.

53 In parallel mode, the complementary strengths of physics-based and ML models—each
54 excelling at different spatiotemporal scales—are leveraged simultaneously. For instance, Niu
55 et al. (2025) incorporated FuXi ML forecasts into the Shanghai Typhoon Model (SHTM) using
56 spectral nudging. By combining FuXi’s large-scale patterns with SHTM’s mesoscale details,
57 this approach substantially improved key typhoon prediction metrics. Similarly, Liu et al.
58 (2023); Liu et al. (2024) demonstrated the WRF-PanGu hybrid model, which emphasized
59 complementarities on the temporal scale. Cremer et al. (2025) extended this idea to
60 hydrologic modeling.

61 In embedded mode, ML is used to represent subgrid and other hard-to-parameterize
62 processes, thereby avoiding the prohibitive computational costs of explicitly resolving them
63 while enhancing accuracy. This approach has become the most common hybridization in
64 climate modeling, with CBRAIN, e.g., (Lin et al., 2023) and CliMA, e.g., (Christopoulos et al.,
65 2024) as notable frameworks. In addition, ClimSim-Online (Yu et al., 2025), an extension of

66 the ClimSim dataset, provides a pipeline for integrating ML models trained on ClimSim into
67 host climate models, further advancing this mode of hybridization.

68 Despite this progress, most hybrid simulations remain confined to single-model systems,
69 such as weather, climate, or ocean models. By contrast, Earth system modeling typically
70 involves multiple interacting components linked through couplers, with each component
71 maintained by independent scientific communities and following distinct development
72 paths. In some data-rich domains, deep learning surrogates have already been adopted—for
73 example, ACE (Watt-Meyer et al., 2023) and CAMulator (Chapman & Berner, 2025) in
74 climate modeling. In other domains, such as land surface (Liu et al., 2025) and hydrologic
75 models (Y. Yang et al., 2025), surrogate development remains immature. Consequently,
76 coupling frameworks must also evolve—from purely physical coupling toward hybrid
77 coupling, in which legacy physics and emerging ML surrogates are integrated, as exemplified
78 by ACE2-SOM (Clark et al., 2024). Surrogate-surrogate coupling approaches also exist, such
79 as DLESyM (Cresswell-Clay et al., 2025) and SamudrACE (Duncan et al., 2025), but fully
80 surrogate-based Earth system models will require additional time to become viable. For the
81 foreseeable future, hybrid coupling of domain-specific models will remain an essential
82 paradigm, though it has yet to receive sufficient attention.

83 The terrestrial water cycle is a critical component of the Earth system. ParFlow, an
84 integrated surface-subsurface hydrologic model, has been widely coupled with land surface
85 and atmospheric models over the past two decades, enabling large-scale simulations of
86 coupled groundwater-land-atmosphere interactions (Yang et al., 2026). However, high-
87 resolution PDE-based simulations are computationally demanding, motivating the recent
88 emergence of ParFlow-based deep learning surrogates (Bennett et al., 2024; Dai et al., 2025;
89 Maxwell et al., 2021; Tran et al., 2021), which accelerate simulations by several hundred to
90 over a thousand times. This study attempts to hybrid-couple a ParFlow surrogate model with
91 the Common Land Model physical model, thereby significantly accelerating the coupled
92 system and enabling rapid forecasts for emergencies such as droughts and floods. Compared
93 to purely surrogate-based models, this hybrid-coupled system retains explicit groundwater-
94 land surface interfaces, ensuring the capacity to investigate groundwater-land interactions.

95 To our knowledge, this is among the first efforts to couple an independent hydrologic
96 surrogate model with a land surface model, demonstrating a practical pathway for
97 integrating data-driven subsurface representations into coupled Earth system simulations.

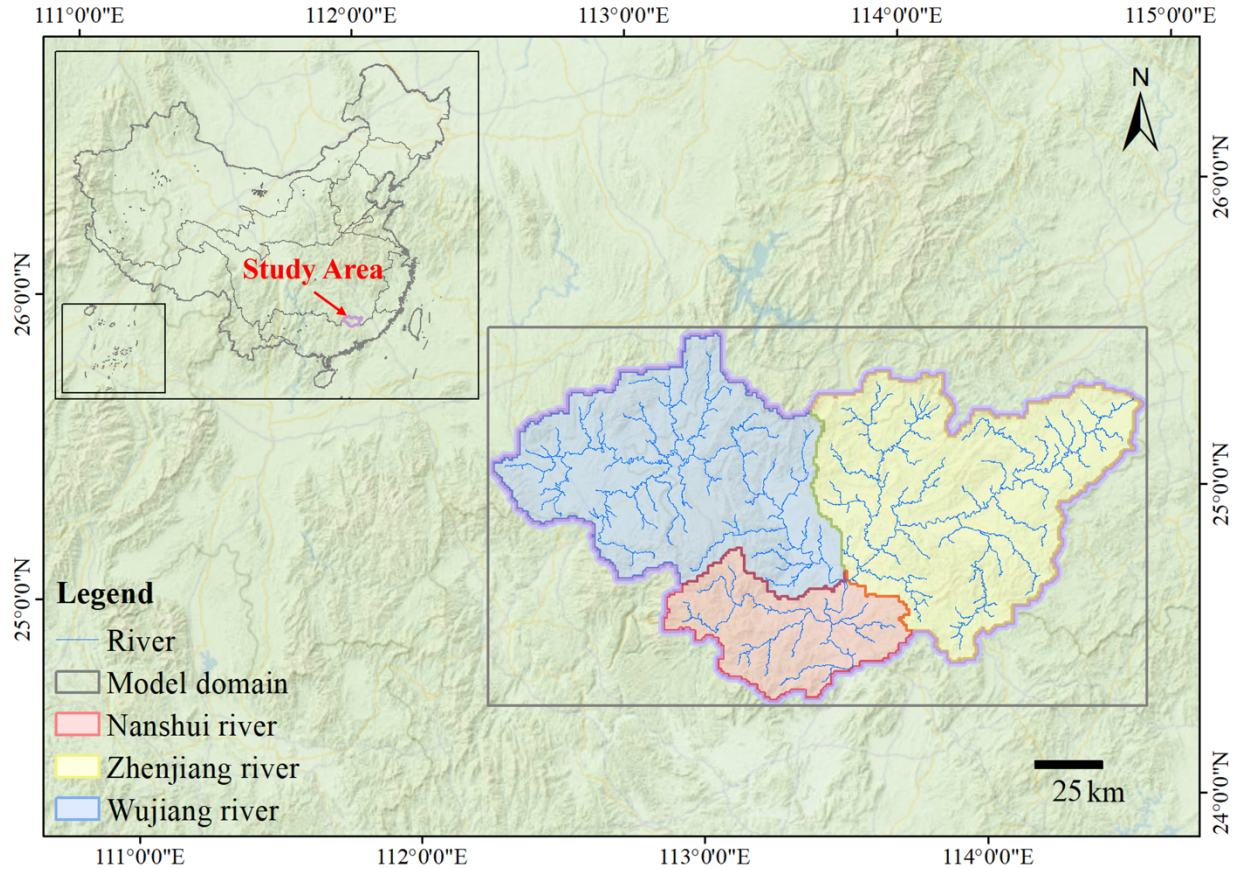
98 Nevertheless, the use of deep-learning surrogates in coupled systems raises several key
99 questions: (1) How does error accumulate over time, and what is the effective forecast
100 horizon? (2) Can the hybrid system faithfully reproduce groundwater–land surface
101 interactions? (3) Does the hybrid system provide meaningful improvement over a simplified
102 lower-bound representation (free drainage), and how can this be used to constrain
103 acceptable model error?

104 **2. Methodology**

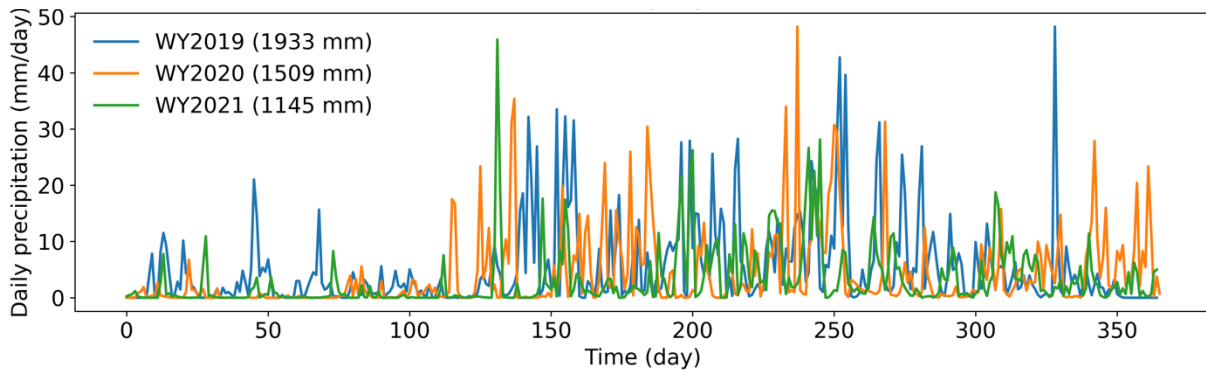
105 **2.1 Physics-based CoLM/ParFlow model**

106 Yang et al. (2026) recoupled ParFlow with the latest version of the Common Land Model
107 (CoLM), achieving improved performance in simulating land surface processes compared
108 with the earlier ParFlow–CLM framework (Maxwell & Miller, 2005). In this configuration,
109 ParFlow and CoLM are coupled through the root zone: ParFlow computes the soil moisture
110 and pressure head required for land surface updates, while CoLM supplies the net fluxes
111 associated with infiltration and evapotranspiration, which are passed to ParFlow as source
112 terms, with flux exchanges performed at an hourly time step.

113 Using this new coupling, a CoLM/ParFlow model was established over a domain in the
114 Pearl River Basin, China, encompassing three humid, monsoon-dominated headwater
115 watersheds, the Zhenjiang River, Wujiang River, and Nanshui River (**Figure 1**). The mean
116 annual precipitation over the study domain is approximately 1527 mm (**Figure 2**) (Muñoz-
117 Sabater et al., 2021). The modeling domain comprises 252×146 grid cells at a horizontal
118 resolution of ~ 1 km, covering an area of approximately 34,000 km². Vertically, the model
119 extends to a depth of 103.43 m, discretized into 11 layers. The upper 10 layers (i.e., the root
120 zone, ~ 3.43 m in total) are consistent with the built-in CoLM soil layers (Yuan & Dai, 2025),
121 while the bottom layer has a thickness of 100 m, representing the deep aquifer.



122
123 **Figure 1. Model domain in the Pearl River Basin, China.** The model domain encompasses three
124 headwater watersheds, including the Zhenjiang River, Wujiang River, and Nanshui River. The domain
125 boundary is shown in purple, and river networks are illustrated in blue. Different colors denote individual
126 watersheds. The inset map indicates the geographic location of the study area within China.



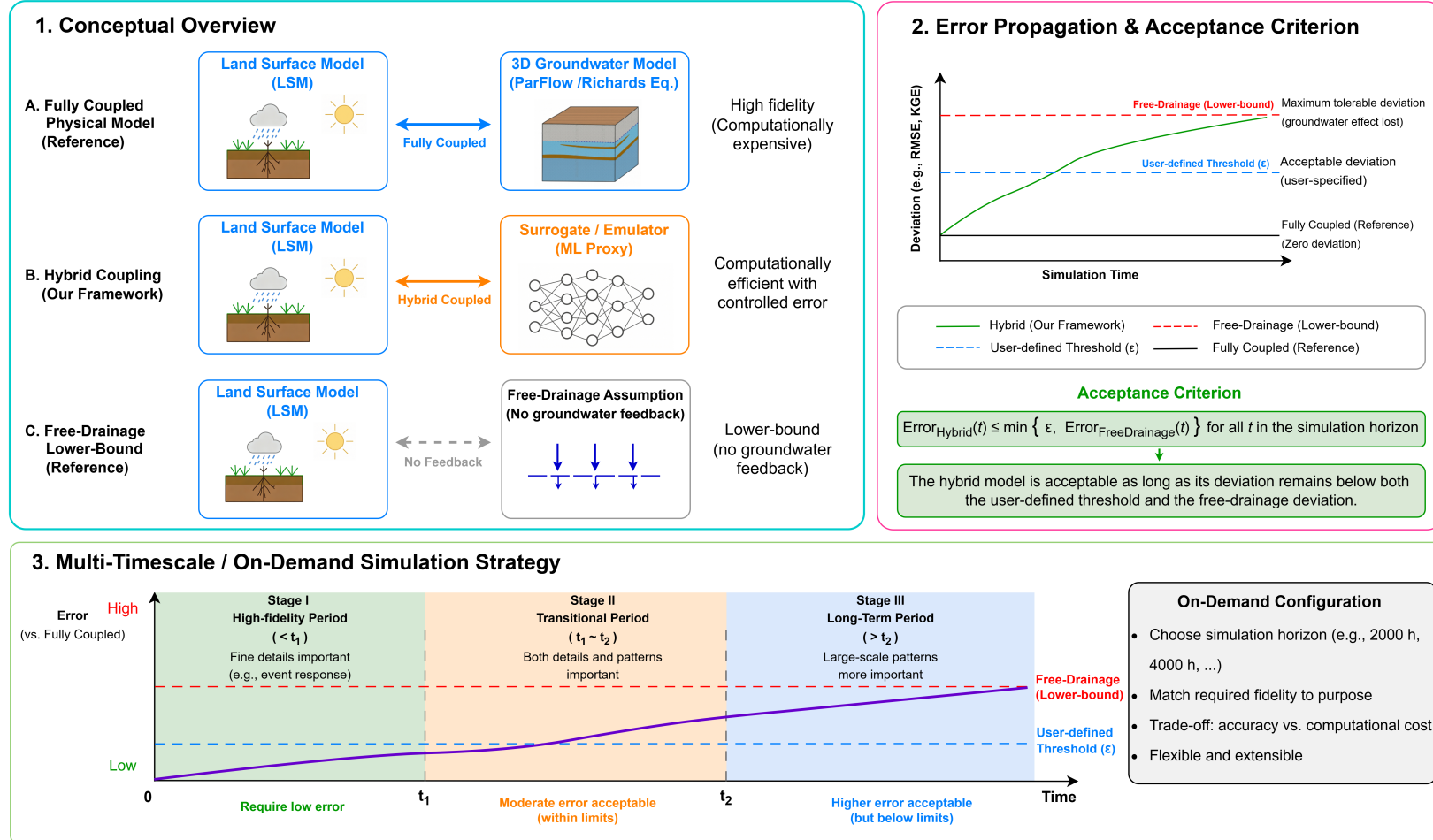
127
128 **Figure 2. Daily precipitation time series aggregated from hourly data over the study region for three**
129 **water years (WY2019–WY2021), used to illustrate hydroclimatic variability.** Total annual
130 precipitation is 1933 mm (WY2019), 1509 mm (WY2020), and 1145 mm (WY2021). Hourly precipitation
131 is used in the model simulations.

132 Soil texture for the upper 10 layers was obtained from the GSDE global dataset
133 (Shangguan et al., 2014), while the permeability of the bottom 100 m layer was derived from

134 the GLHYMPS global dataset and further adjusted using an e -folding decay function with
135 depth and slope (Fan et al., 2007; Gleeson et al., 2011). Land cover information was taken
136 from the MODIS MCD12Q1.061 product (Friedl & Sulla-Menashe, 2022). Terrain slope was
137 calculated from a digital elevation model (DEM) after applying hydrological processing to
138 ensure flow connectivity (Eilander et al., 2021). Both slope and land cover datasets were
139 adopted from the national-scale CONCN model (C. Yang et al., 2025). All original datasets
140 were reprojected and interpolated to match the model grid and resolution. Lateral and
141 bottom boundary conditions were prescribed as no-flow boundaries.

142 For each watershed, the initial condition was specified with a uniform water table depth
143 (WTD) of 2 m. The model was first driven by multi-year mean precipitation minus
144 evapotranspiration (P-ET), derived from the national-scale CONCN model, to reach a quasi-
145 equilibrium state, defined as a condition where the change in total water storage is less than
146 1% of the cumulative P-ET over the corresponding period (C. Yang et al., 2025).
147 Subsequently, the land surface model (CoLM) was activated, and the coupled system was
148 forced using meteorological data from water year (WY) 2019 (October–September) derived
149 from the ERA5-Land reanalysis (Muñoz-Sabater et al., 2021) for a four-year spin-up to
150 achieve dynamic equilibrium. The model was then driven by meteorological forcings from
151 WY2020 and WY2021 for subsequent simulations.

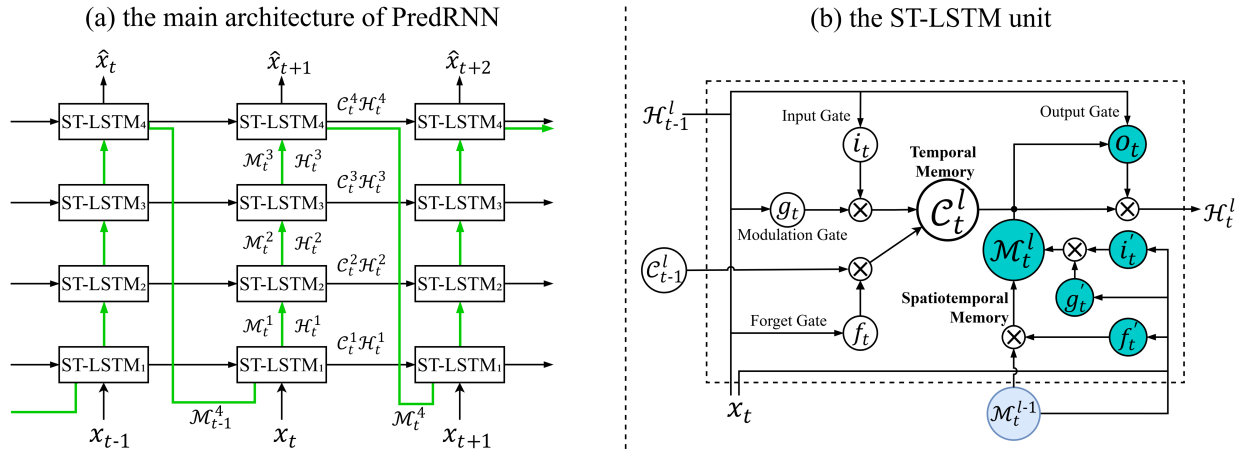
152 In addition, we constructed an alternative configuration in which lateral groundwater
153 flow was disabled and the bottom boundary condition was changed from a no-flow boundary
154 to a free-drainage boundary. This setup approximates the treatment of subsurface processes
155 commonly adopted in traditional land surface models, where groundwater feedback is
156 largely neglected. This configuration serves as a lower-bound benchmark for evaluating the
157 hybrid coupling system (**Figure 3**). Specifically, if the discrepancies between the hybrid
158 coupling and the fully coupled physical model are not greater than those between the free-
159 drainage configuration and the fully coupled model, it suggests that the hybrid approach is
160 able to capture, to some extent, the influence of groundwater on land surface processes.



161
 162 **Figure 3. Conceptual framework of the hybrid groundwater–land surface coupling system. (1) Conceptual overview:** comparison between the
 163 fully coupled physical model (reference), the proposed hybrid coupling using a surrogate/emulator, and the free-drainage configuration
 164 representing a lower-bound case without groundwater feedback. **(2) Error propagation and acceptance criterion:** deviation of the hybrid system
 165 relative to the fully coupled reference is evaluated over time. The hybrid solution is considered acceptable as long as its error remains below both
 166 a user-defined threshold and the free-drainage lower-bound deviation, ensuring that essential groundwater effects are retained. **(3) Multi-**
 167 **timescale/on-demand simulation strategy:** the framework enables flexible simulation across different temporal horizons, where high fidelity is
 168 maintained for short-term dynamics, while larger errors are tolerated for long-term simulations within defined bounds, allowing a trade-off
 169 between accuracy and computational efficiency.

170 2.2 ParFlow deep-learning surrogate model

171 The ParFlow surrogate model developed in this study is a deep learning architecture
 172 adapted from FSTR (Bennett et al., 2024), itself a variant of PredRNN (Wang et al., 2022).
 173 The surrogate is designed to emulate the physics-based ParFlow model by predicting the 3D
 174 pressure head field at each timestep, given the initial pressure head, static parameters (e.g.,
 175 soil properties), and dynamic external inputs (root-zone net fluxes provided by CoLM). In
 176 this study, the term “external inputs” refers specifically to root-zone net fluxes provided by
 177 the land surface model, rather than raw meteorological forcings. For surrogate training and
 178 validation, these net fluxes were obtained from CoLM/ParFlow simulations forced by
 179 meteorological data. The resulting root-zone net fluxes were extracted and used as dynamic
 180 inputs to the surrogate model. The predicted pressure head can then be used to derive WTD
 181 and, in combination with soil hydraulic parameters, to estimate soil moisture through the
 182 van Genuchten (VG) model (van Genuchten, 1980).



183
 184 **Figure 4. Architecture of the PredRNN model and the spatiotemporal LSTM (ST-LSTM) unit (Wang et**
 185 **al., 2022).** (a) Overall architecture, illustrating the stacked ST-LSTM layers and the flow of temporal and
 186 spatiotemporal memories (C_t^l and M_t^l) across timesteps. (b) Structure of a single ST-LSTM unit, showing
 187 the interactions between temporal memory, spatiotemporal memory, and the gating mechanisms that
 188 control information propagation.

189 The core architecture of the PredRNN-based surrogate is illustrated in **Figure 4**. The left
 190 panel presents the stacked spatiotemporal LSTM (ST-LSTM) structure and the
 191 spatiotemporal memory (\mathcal{M}) flow across layers and timesteps, while the right panel shows
 192 the detailed structure of a single ST-LSTM unit. The corresponding mathematical

193 formulations of the ST-LSTM and the action-conditioned mechanism are given below. In the
 194 equations, t denotes the current timestep, and l indicates the layer index in the stacked ST-
 195 LSTM architecture. The operator $*$ represents convolution, and \odot denotes element-wise
 196 multiplication. The terms W_{\cdot} denote learnable convolutional kernels, and $\sigma(\cdot)$ and $\tanh(\cdot)$
 197 represent the sigmoid and hyperbolic tangent activation functions, respectively. In the
 198 action-conditioned mechanism, \mathcal{V}_t^l can be interpreted as an action-modulated
 199 representation of the previous hidden state \mathcal{H}_{t-1}^l , where the external forcing \mathcal{A}_{t-1} is
 200 incorporated to influence the state transition.

$$201 \quad g_t = \tanh(W_{xg} * \mathcal{X}_t + W_{hg} * \mathcal{H}_{t-1}^l)$$

$$202 \quad i_t = \sigma(W_{xi} * \mathcal{X}_t + W_{hi} * \mathcal{H}_{t-1}^l)$$

$$203 \quad f_t = \sigma(W_{xf} * \mathcal{X}_t + W_{hf} * \mathcal{H}_{t-1}^l)$$

$$204 \quad \mathcal{C}_t^l = f_t \odot \mathcal{C}_{t-1}^l + i_t \odot g_t$$

$$205 \quad g'_t = \tanh(W'_{xg} * \mathcal{X}_t + W_{mg} * \mathcal{M}_t^{l-1})$$

$$206 \quad i'_t = \sigma(W'_{xi} * \mathcal{X}_t + W_{mi} * \mathcal{M}_t^{l-1})$$

$$207 \quad f'_t = \sigma(W'_{xf} * \mathcal{X}_t + W_{mf} * \mathcal{M}_t^{l-1})$$

$$208 \quad \mathcal{M}_t^l = f'_t \odot \mathcal{M}_t^{l-1} + i'_t \odot g'_t$$

$$209 \quad o_t = \sigma(W_{xo} * \mathcal{X}_t + W_{ho} * \mathcal{H}_{t-1}^l + W_{co} * \mathcal{C}_t^l + W_{mo} * \mathcal{M}_t^l)$$

$$210 \quad \mathcal{H}_t^l = o_t \odot \tanh(W_{1 \times 1} * [\mathcal{C}_t^l, \mathcal{M}_t^l])$$

$$211 \quad \text{Action fusion: } \mathcal{V}_t^l = (W_{hv} * \mathcal{H}_{t-1}^l) \odot (W_{av} * \mathcal{A}_{t-1})$$

$$212 \quad \mathcal{H}_t^l, \mathcal{C}_t^l, \mathcal{M}_t^l = \text{ST-LSTM}(\mathcal{X}_t, \mathcal{V}_t^l, \mathcal{C}_{t-1}^l, \mathcal{M}_t^{l-1})$$

213 Building upon the standard PredRNN formulation, we introduce several modifications
214 following FSTR to enable its application as a surrogate model. Specifically, convolutional
215 encoders are employed to process static parameters and the initial pressure head field,
216 which are used to initialize both the temporal memory \mathcal{C} and the spatiotemporal memory
217 \mathcal{M} . The static inputs are constructed from hydrogeological parameters across all vertical
218 layers. Specifically, four soil parameters—permeability, porosity, and the van Genuchten
219 parameters (α and n)—are included for each of the 11 layers, resulting in 44 channels. In
220 addition, two surface-related parameters, slope and Manning’s coefficient, are incorporated,
221 yielding a total of 46 static input channels. These parameters are encoded once and used to
222 initialize the memory states (\mathcal{C}) of the network.

223 Following FSTR, we adopt an autoregressive scheme in which the predicted pressure
224 head field from the previous timestep is directly used as the input \mathcal{X}_t for the next timestep.
225 This design avoids the use of scheduled sampling in PredRNN, where ground-truth and
226 predicted states are mixed during training (Wang et al., 2022). External inputs are
227 incorporated through the action-conditioned design in PredRNN. In this study, the actions
228 correspond to root-zone net fluxes provided by the physics-based CoLM/ParFlow model
229 (**Section 2.1**), representing the combined effects of infiltration and evapotranspiration. By
230 adopting this flux-based interface, the surrogate model remains consistent with the input-
231 output structure of the ParFlow model, enabling seamless coupling with the land surface
232 model. During coupled simulations, fluxes computed by CoLM can be directly supplied to the
233 surrogate model, allowing it to advance subsurface states in a manner consistent with the
234 original physics-based system. This differs from the original FSTR formulation, where the
235 surrogate is trained in an end-to-end manner using meteorological forcings as inputs.

236 Additional adaptations were made to account for structural differences between the
237 earlier ParFlow-CLM configuration used in FSTR and the updated version applied in this
238 study. Specifically, the new CoLM/ParFlow model includes 10 coupled layers, resulting in
239 input channel dimensions of 11, 10, and 46 for the initial condition, external inputs, and static
240 parameters, respectively, compared with 5, 5, and 15 in FSTR. Despite the increased input
241 dimensionality, we retain the original hidden-state size of 16 channels used in FSTR, rather

242 than increasing the hidden-state dimensionality of the ST-LSTM layers. This design implicitly
243 requires the network to encode high-dimensional inputs into a compact latent
244 representation. In addition, while FSTR used a convolutional kernel size of 5, we found that
245 a kernel size of 3 yields better performance in our experiments. This improvement may be
246 related to the characteristic spatial correlation scales of groundwater dynamics. These
247 design choices improve predictive performance while substantially reducing the number of
248 trainable parameters. As a result, the final model contains approximately 86K trainable
249 parameters, less than half that of the original FSTR model (194K parameters).

250 The model was trained using data from WYs 2019–2020, while the first 720 hours of
251 WY2021 were used for validation, and the full year of WY2021 was used for subsequent
252 evaluation. The model domain was partitioned into non-overlapping patches of size 16×16 .
253 For domains where the spatial dimensions are not exact multiples of the patch size,
254 additional patches were extracted from the domain boundaries to ensure full spatial
255 coverage. A rollout horizon of 120 hours was employed without overlap for training and
256 validation, yielding 23,360 training samples and 960 validation samples. This horizon was
257 chosen to balance temporal dependency learning and computational cost. The model
258 predicts pressure head fields at the patch level, which are then reassembled to reconstruct
259 the full domain.

260 Model training was conducted using the AdamW optimizer with a OneCycle learning rate
261 schedule. The learning rate increased from 4×10^{-4} to 2×10^{-3} during the first 30% of training,
262 and then decreased to 8×10^{-5} for the remaining iterations. A batch size of 16 was used. The
263 loss function consists of a mean squared error (MSE) term between the predicted and
264 reference pressure head fields and an additional penalty on the horizontal gradients of the
265 predicted pressure head field, with a weighting factor of 0.1, to enforce spatial smoothness.
266 Static parameters were standardized using their spatial mean and standard deviation for
267 each vertical layer. Pressure heads were standardized using the mean and standard
268 deviation computed from the two-year training period for each vertical layer. Net fluxes
269 were standardized using the mean and standard deviation computed from the same training
270 period. Training was performed for approximately 8×10^4 iterations (about 55 epochs). To

271 reduce the influence of stochastic variability, the training process was repeated five times.
272 In two of these runs, training was further continued for an additional 8×10^4 iterations at a
273 fixed learning rate of 8×10^{-5} ; however, no significant improvement in loss was observed. The
274 model with the best validation performance was selected for subsequent evaluation. All
275 experiments were conducted on a single NVIDIA A100 GPU (80 GB).

276 **2.3 Additional architectural experiments**

277 To further explore the potential for improving surrogate performance, we conducted
278 additional experiments by introducing attention mechanisms into the model architecture.
279 Inspired by recent spatiotemporal attention studies (Lim et al., 2021; Xiong et al., 2024;
280 Zheng et al., 2021), we implemented a temporal self-attention module between the final
281 hidden layer and the output layer. Prior to applying attention, the spatial dimensions of the
282 hidden states were compressed while preserving channel-wise information. Two alternative
283 modes were considered. In the pooling mode, global adaptive average pooling was applied
284 to each hidden feature map, reducing the spatial grids to a channel-wise representation. In
285 the xyconv mode, two depthwise convolutions with kernel sizes and strides equal to the
286 patch size were used to compress the spatial dimensions to a single location—first along the
287 y-direction and then along the x-direction—yielding a learnable spatial aggregation of each
288 feature channel. Both modes were retained in the implementation to facilitate flexible
289 adaptation to different applications.

290 The resulting channel embeddings across time steps were then fed into a temporal self-
291 attention module, where the current timestep was used as the query and all preceding
292 timesteps (including the current one) as keys and values. The attention weights were used
293 to reweight the stacked hidden states across time, assigning a scalar importance to each
294 timestep’s spatial feature map. The weighted hidden states were then aggregated to produce
295 an attention-enhanced spatiotemporal representation, which was subsequently passed
296 through the output convolution layer for prediction. A learnable scaling factor was applied
297 to modulate the contribution of the attention-enhanced features before being added to the
298 original prediction.

299 Preliminary experiments with the attention-enhanced architecture (**Figure S1**) showed
300 performance comparable to that of the baseline model in terms of both training loss and
301 validation RMSE. This indicates that the PredRNN-based architecture already captures the
302 dominant spatiotemporal dependencies in this application, leaving limited room for further
303 improvement through additional attention modules. Given that the primary objective of this
304 study is to demonstrate the feasibility of coupling the ParFlow surrogate with the physics-
305 based CoLM model, we did not pursue further architectural refinements. Nevertheless,
306 future work may explore alternative architectures, such as transformer-based models, for
307 broader applications.

308 **2.4 ParFlow surrogate–CoLM physics hybrid coupling**

309 The trained ParFlow surrogate was coupled with the physics-based CoLM in an online
310 hybrid framework to reproduce the behavior of the fully physics-based coupled system. In
311 this framework, CoLM and the surrogate exchange information dynamically at every
312 timestep: CoLM provides root-zone net fluxes, and the surrogate predicts the updated three-
313 dimensional pressure head field. Saturation is subsequently derived from the predicted
314 pressure head through the van Genuchten (VG) relationship. Both the updated pressure
315 head and the derived saturation are then passed back to CoLM for the next timestep. To
316 enable this two-way coupling, the standalone surrogate was reformulated from a multi-step
317 predictor driven by prescribed net fluxes to a single-step autoregressive model. At each
318 timestep, the surrogate takes the current subsurface state together with the corresponding
319 CoLM-generated net fluxes and advances the pressure head field by one step. This
320 modification allows the surrogate to be embedded directly within the online coupling loop,
321 ensuring synchronous state updates between the two components.

322 From an implementation perspective, CoLM was compiled as a shared library and
323 exposed through a Fortran–C interface using BIND(C), which provides a C-compatible entry
324 point for its land surface routines. This interface allows the compiled library to be directly
325 invoked from external Python code during online coupling. It forms the foundation of the
326 hybrid implementation, enabling seamless integration of CoLM physics within the surrogate
327 prediction loop. To preserve consistency with the original physics-based coupled model and

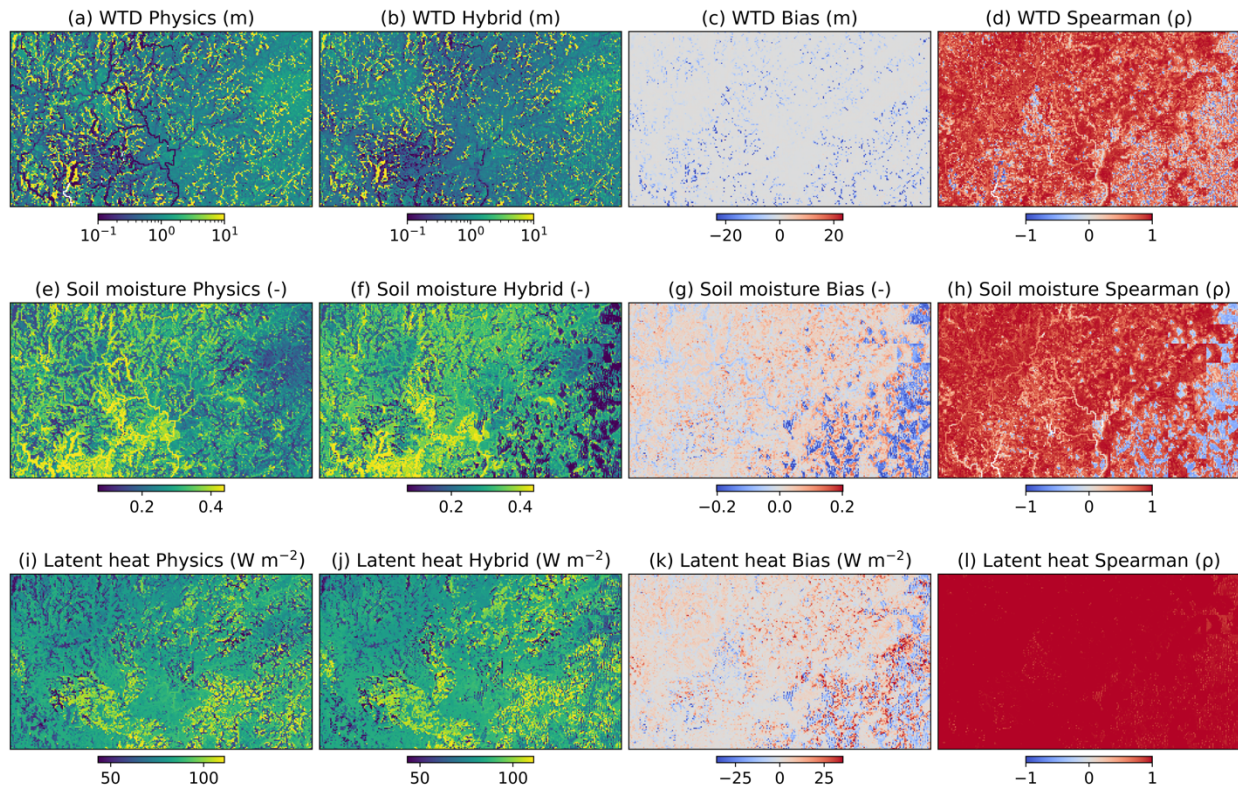
328 to enable a fair assessment of computational efficiency, the CoLM component retained the
329 same domain decomposition strategy as the fully physics-based system. In the physics-based
330 model, the domain is partitioned according to its parallel spatial decomposition, which
331 depends on both the domain size and the number of subdivisions specified in each horizontal
332 direction. For example, the model domain is divided into 4 partitions along the x-direction
333 and 3 along the y-direction, resulting in 12 spatial blocks and thus 12 parallel processes.

334 Based on this block structure, parallel execution was implemented in Python by assigning
335 each block to a dedicated worker process. Each worker loaded an independent CoLM shared-
336 library instance and advanced the land surface calculations for its assigned block. Within
337 each worker, meteorological forcings were loaded one day at a time and cached locally to
338 reduce repeated I/O overhead, while still being applied at the native hourly timestep during
339 simulation. The surrogate, by contrast, operates on fixed-size spatial patches (16×16)
340 consistent with its training configuration. After each timestep, the block-wise CoLM outputs
341 were first assembled back to the full domain and then reshaped into surrogate input patches
342 for the next prediction step. The hybrid system was evaluated over the full WY2021,
343 following surrogate training on water years 2019–2020 and validation over the first 720
344 hours of 2021. This setup allows evaluation of both predictive performance and long-term
345 stability of the coupled system under realistic forcing conditions.

346 **3. Results and discussion**

347 To assess training robustness, the surrogate model was trained five times with different
348 random initializations (**Figure S2**). All runs showed a similar optimization pattern, with a
349 rapid decrease in both training loss and validation RMSE during the early stage, followed by
350 gradual convergence to similar plateau levels. At the same time, the trajectories were not
351 identical: some runs exhibited more pronounced intermediate fluctuations, particularly in
352 validation RMSE, indicating moderate sensitivity to initialization during optimization. For
353 selected runs, training was further extended beyond approximately 8×10^4 iterations at a
354 fixed learning rate of 8×10^{-5} , but this resulted in little additional improvement in validation
355 performance, indicating that the model had effectively converged. The checkpoint with the
356 lowest validation RMSE was therefore chosen for subsequent evaluation.

357 In terms of computational efficiency, the standalone surrogate model achieves an
358 approximate $100\times$ speedup relative to the fully physics-based coupled simulation. When
359 embedded within the land surface coupling framework, the resulting hybrid system still
360 yields an overall speedup of approximately $20\times$ compared to the fully physics-based coupled
361 model. Further optimization (e.g., implementation-level improvements) could potentially
362 lead to additional gains, but this is beyond the scope of the present study.

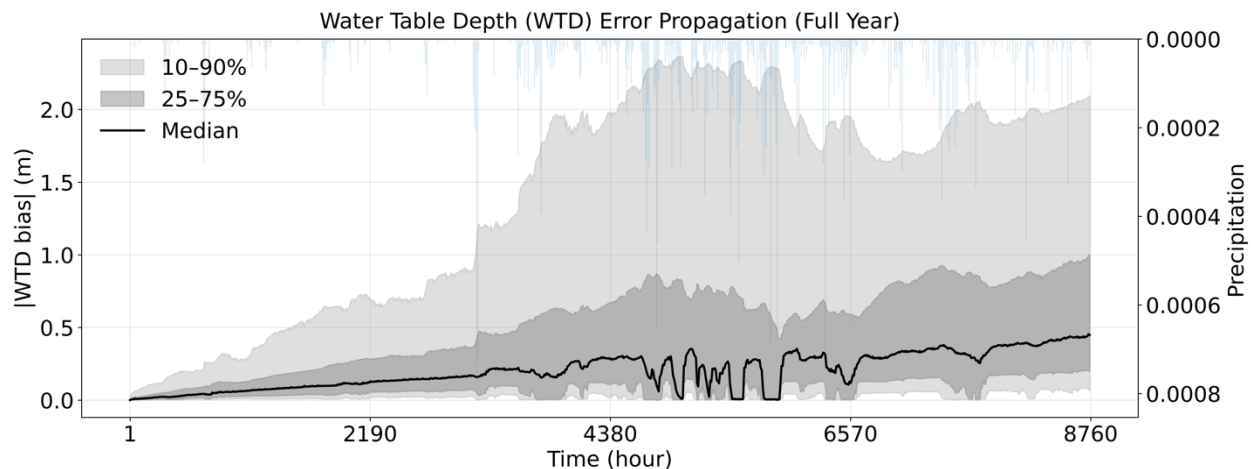


363
364 **Figure 5. Spatial distributions of annual mean states and corresponding model agreement between**
365 **the physics-based and hybrid models.** The first, second, and third rows correspond to water table depth
366 (WTD), near-surface soil moisture (top layer), and latent heat flux, respectively. For each variable, the
367 columns show: (a, e, i) the physics-based model, (b, f, j) the hybrid model, (c, g, k) the bias, and (d, h, l) the
368 Spearman rank correlation coefficient (ρ) computed from the temporal series at each grid cell. The bias is
369 defined as hybrid minus physics, such that positive values indicate overestimation by the hybrid model
370 relative to the physics-based model, and negative values indicate underestimation. Spearman correlation
371 quantifies the temporal agreement between the two models at each grid cell, with values close to 1
372 indicating strong monotonic consistency.

373 The spatial distributions of WTD, soil moisture, and latent heat exhibit clear patterns
374 controlled by underlying physical factors (**Figure 5**). WTD shows strong topographic control,
375 with shallow water tables concentrated along river networks and valley bottoms, and deeper
376 groundwater levels distributed over upland regions. Soil moisture broadly follows this

377 pattern, reflecting the influence of groundwater proximity on near-surface water availability.
378 At the same time, soil moisture and latent heat are additionally modulated by soil texture
379 and land surface properties, leading to finer-scale spatial heterogeneity beyond the
380 topographic signal. In particular, variations in soil hydraulic properties and vegetation-
381 related processes introduce spatial variability that is not solely explained by groundwater
382 dynamics (**Figure S3**).

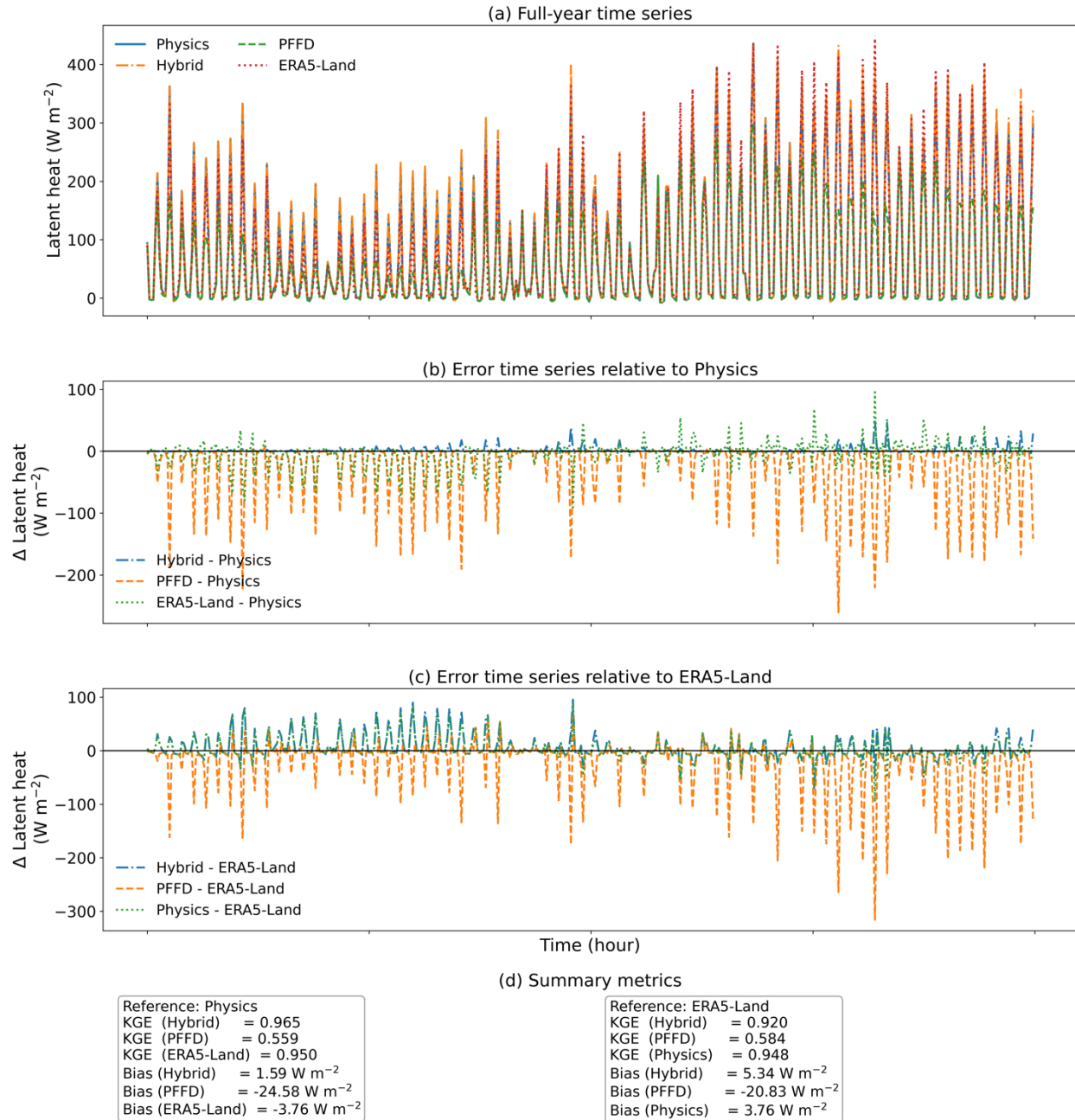
383 The hybrid model reproduces the overall spatial patterns of all three variables well,
384 indicating that it successfully captures the dominant large-scale controls. However,
385 noticeable discrepancies appear in certain regions, particularly in the southeastern part of
386 the domain, where both WTD and soil moisture exhibit localized distortions compared to the
387 physics-based model. These inconsistencies propagate into the latent heat flux, resulting in
388 larger biases in the same region. Consistent with these spatial deviations, the temporal
389 agreement between the hybrid and physics-based models, as measured by the Spearman
390 correlation, is slightly reduced in these areas. This suggests that errors in subsurface states
391 can propagate upward, affecting both the magnitude and timing of surface fluxes.



392
393 **Figure 6. Temporal evolution of water table depth (WTD) bias and its variability over 8760 hours (one**
394 **full year).** The black line represents the median absolute WTD bias across all grid cells at each time step,
395 while the shaded regions denote the interquartile range (25–75%) and the broader distribution (10–
396 90%), respectively. The blue curve (right axis) shows precipitation, providing the primary external forcing
397 to the system.

398 **Figure 6** illustrates the temporal evolution of WTD bias and its variability over a full year
399 (8760 hours), summarized by the median and percentile ranges. Overall, the median WTD
400 bias remains relatively small throughout the simulation, generally staying within ~ 0.5 m,
401 indicating that the hybrid model maintains a reasonable level of accuracy over time.
402 However, the median bias increases gradually, suggesting a progressive accumulation of
403 errors during the autoregressive prediction. At the same time, the spread of the bias
404 distribution widens substantially: the interquartile range (25–75%) expands from near-zero
405 at the beginning to approximately 0.2–1.0 m, while the 10–90% range grows to over ~ 2 m
406 in the later stages, reflecting increasingly dispersed errors in the hybrid system. Notably,
407 periods of increased precipitation coincide with a pronounced expansion of the bias range,
408 during which both the median and upper quantiles exhibit sharper excursions. This indicates
409 that errors in the hybrid model become more variable under strong hydrological forcing,
410 suggesting reduced robustness of the neural network component in capturing rapid state
411 transitions associated with precipitation events.

412 **Figure 7** shows the domain-averaged latent heat flux time series for different model
413 configurations, together with their deviations from both the physics-based model and ERA5-
414 Land, as well as summary performance metrics. The hybrid model closely follows the
415 physics-based simulation throughout the entire period, while the PFFD configuration
416 exhibits substantially larger deviations, particularly during high-flux periods. This behavior
417 is likely associated with the absence of groundwater feedback in the PFFD configuration,
418 which limits the ability of the system to sustain evapotranspiration under conditions of high
419 atmospheric demand, leading to a more water-limited regime. ERA5-Land captures the
420 general temporal variability and shows a comparable level of agreement with the physics-
421 based model. The physics-based model is used as a common reference to enable consistent
422 comparison across datasets, and the metrics reported here (e.g., KGE) quantify agreement
423 rather than absolute accuracy.



424

425 **Figure 7. Comparison of domain-averaged latent heat flux across different modeling configurations**
 426 **and references.** (a) Full-year time series of latent heat flux from the physics-based model, the hybrid
 427 model, the free-drainage (PFFD) configuration, and the ERA5-Land reanalysis. (b) Error time series
 428 relative to the physics-based model (Hybrid – Physics, PFFD – Physics, and ERA5-Land – Physics). (c)
 429 Error time series relative to ERA5-Land (Hybrid – ERA5-Land, PFFD – ERA5-Land, and Physics – ERA5-
 430 Land). (d) Summary metrics, including Kling–Gupta efficiency (KGE) and mean bias, computed with
 431 respect to both the physics-based model and ERA5-Land. To improve readability, the time series is
 432 subsampled and plotted at 20-hour intervals.

433

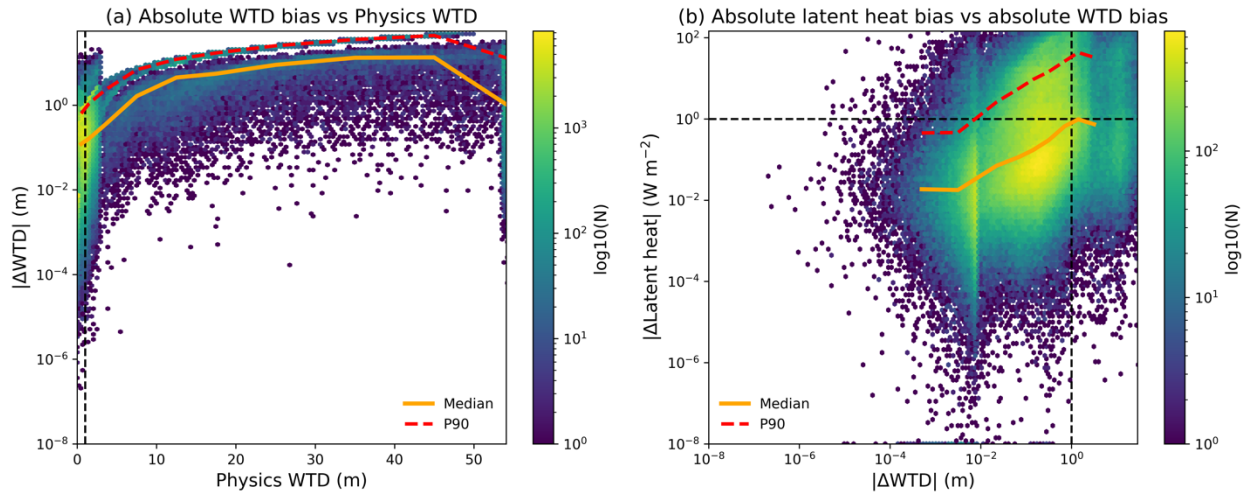
434 As an additional point of reference, we include the ERA5-Land reanalysis, which, although
435 lacking an explicit groundwater representation, is constrained by observations through data
436 assimilation. ERA5-Land shows relatively good agreement with the physics-based model,
437 with a high KGE and low bias, indicating that both datasets capture consistent large-scale flux
438 dynamics. This agreement does not imply that ERA5-Land should match the physics-based
439 model, but rather suggests that the physics-based simulation is consistent with an
440 observation-constrained estimate. In this context, the agreement between the two provides
441 indirect support for the importance of groundwater processes in reproducing realistic land-
442 atmosphere fluxes.

443 In contrast, the free-drainage configuration (PFFD) shows substantially larger deviations
444 from the physics-based model. Latent heat flux is systematically underestimated, and this
445 bias is further supported by the spatial patterns shown in **Figure S4**, where PFFD exhibits
446 uniformly lower fluxes across the domain. Despite this bias, PFFD captures the general
447 temporal variability, as reflected in both its reasonable timing (**Figure 7**) and its relatively
448 high Spearman correlation (**Figure S4**), but yields a substantially lower KGE, indicating that
449 neglecting groundwater primarily affects flux magnitude rather than temporal structure.

450 The hybrid model, by comparison, maintains a high level of agreement with the physics-
451 based simulation throughout the entire period, achieving a KGE close to unity and exhibiting
452 much smaller errors than PFFD. As discussed in **Section 2.1** or **Figure 3**, a necessary
453 condition for the hybrid model to capture groundwater feedback is that its error remains
454 within the deviation introduced by the free-drainage assumption. The hybrid model clearly
455 satisfies this criterion, with errors substantially smaller than those of PFFD. Together with
456 the consistency between the physics-based model and ERA5-Land, these results indicate that
457 the hybrid model successfully captures the key groundwater-land surface interactions
458 governing latent heat flux.

459 The temporal analysis (**Figures 6 and 7**) suggests a clear co-variation between
460 subsurface and surface errors. In particular, periods with larger WTD biases—such as around
461 hour ~4380 and after hour ~6570—are consistently associated with amplified deviations in
462 latent heat flux, indicating a potential propagation of errors from groundwater states to

463 surface fluxes. However, domain-averaged time series cannot fully capture the spatial
464 variability of this relationship. To further examine how groundwater-related errors are
465 associated with flux biases, we extend the analysis to the grid-cell level by analyzing the joint
466 distribution of WTD and latent heat errors.



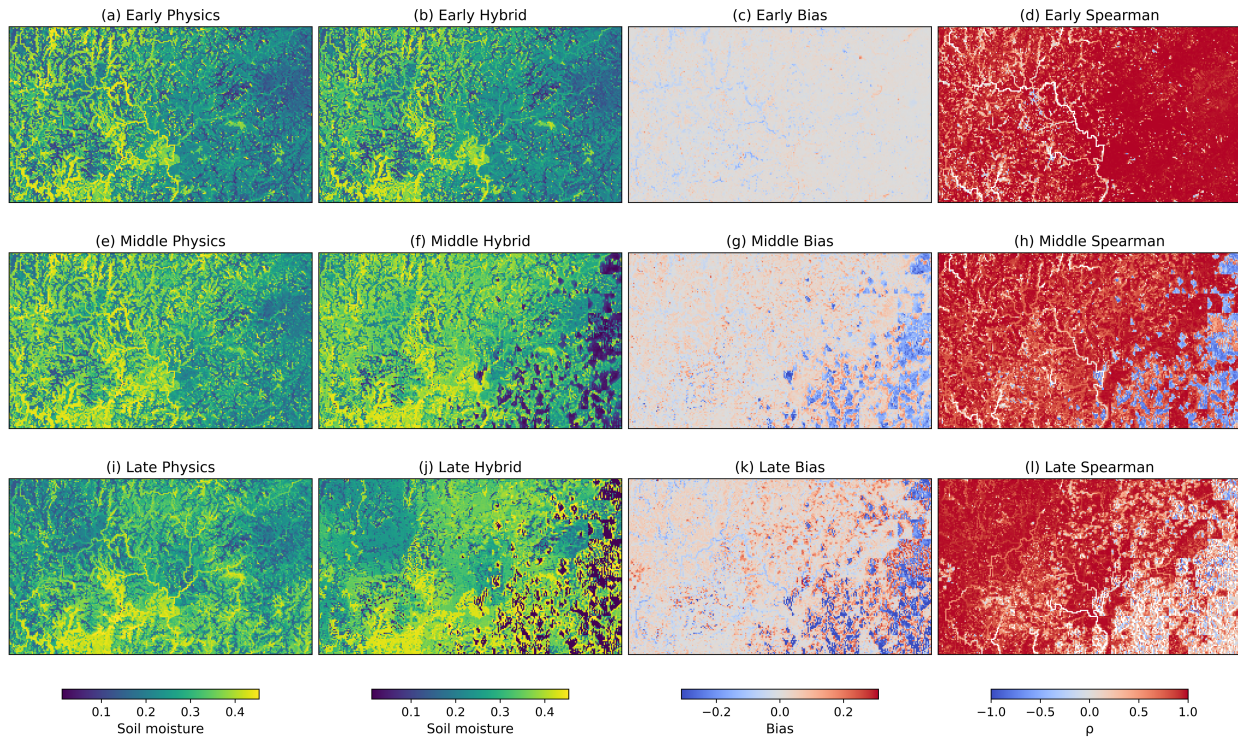
467
468 **Figure 8. Relationship between groundwater-related errors and their propagation to surface fluxes.**
469 (a) Absolute water table depth (WTD) bias as a function of physics-based WTD. Colors indicate point
470 density (\log_{10} scale). The solid orange line shows the median, and the dashed red line shows the 90th
471 percentile within each WTD bin. The vertical dashed line at 1 m indicates the transition between shallow
472 and deep groundwater regimes. (b) Absolute latent heat bias as a function of absolute WTD bias, shown
473 on logarithmic axes. Colors indicate point density (\log_{10} scale), with median and 90th percentile trends
474 overlaid.

475 To characterize the relationship between groundwater-related errors and their
476 propagation to surface fluxes, we constructed a paired dataset by comparing the hybrid
477 model outputs against the fully physics-based CoLM/ParFlow simulations over WY2021. At
478 each grid cell and timestep, WTD and latent heat flux differences were computed, yielding
479 Δ WTD and Δ Latent heat. These paired samples were collected across randomly sampled
480 timesteps and grid cells and combined into a dataset spanning the entire domain and
481 simulation period. The relationships were analyzed using density-based binning to highlight
482 the distribution of sample points (**Figure 8**). Results show that WTD bias increases
483 systematically with increasing WTD, indicating reduced model accuracy under deeper water
484 table conditions. In addition, latent heat bias exhibits a clear positive relationship with WTD
485 bias, demonstrating that errors in subsurface states propagate upward and can be amplified
486 in surface fluxes.

487 Most samples are concentrated around WTD ≈ 1 m, corresponding to a transition toward
488 an energy-limited regime. In this range, WTD biases are generally below 1 m and are
489 associated with relatively small latent heat errors, as reflected by the median relationship
490 (yellow curve) remaining below $\sim 1 \text{ W m}^{-2}$. However, a subset of samples exhibits
491 substantially larger latent heat errors, reaching values close to 100 W m^{-2} . The median and
492 upper quantile relationships (yellow and red curves) exhibit an approximate power-law
493 scaling between latent heat bias and WTD bias over the range of 10^{-2} to 1 m, indicating a
494 nonlinear amplification of subsurface errors in the dominant regime. Importantly, these large
495 flux errors (up to $\sim 100 \text{ W m}^{-2}$) are confined to a relatively small subset of samples and are
496 associated with conditions where surface fluxes are highly sensitive to groundwater
497 dynamics, rather than representing the dominant system behavior. This behavior can be
498 interpreted in the context of the critical depth theory of groundwater–land surface
499 interactions (Kollet & Maxwell, 2008; Yang et al., 2020). When WTD exceeds approximately
500 10 m, groundwater influence on surface fluxes becomes negligible; consequently, even large
501 WTD errors in these regions have limited impact on latent heat flux. In contrast, within the
502 shallow groundwater regime, where capillary connections are active, relatively small WTD
503 errors can lead to disproportionately large surface flux deviations. This explains why most
504 samples exhibit small errors, while a limited subset produces large flux biases.

505 To investigate how errors propagate over time under meteorological forcing, we divide
506 the simulation period into three stages: early, middle, and late (**Figures 9, S5, and S6**).
507 During the early stage, the hybrid model closely matches the physics-based simulation,
508 successfully capturing both large-scale spatial patterns and fine-scale heterogeneity,
509 indicating an accurate representation of groundwater–land surface coupling. In the middle
510 stage, deviations begin to emerge, particularly in localized regions (e.g., the southeastern
511 part of the domain). While the overall spatial pattern remains consistent with the physics-
512 based model, fine-scale structures are partially degraded, suggesting that accumulated
513 subsurface errors start to influence surface variables. By the late stage, this degradation
514 becomes more pronounced: the hybrid model largely preserves dominant large-scale
515 patterns, while fine-scale spatial variability is substantially lost. Correspondingly, the

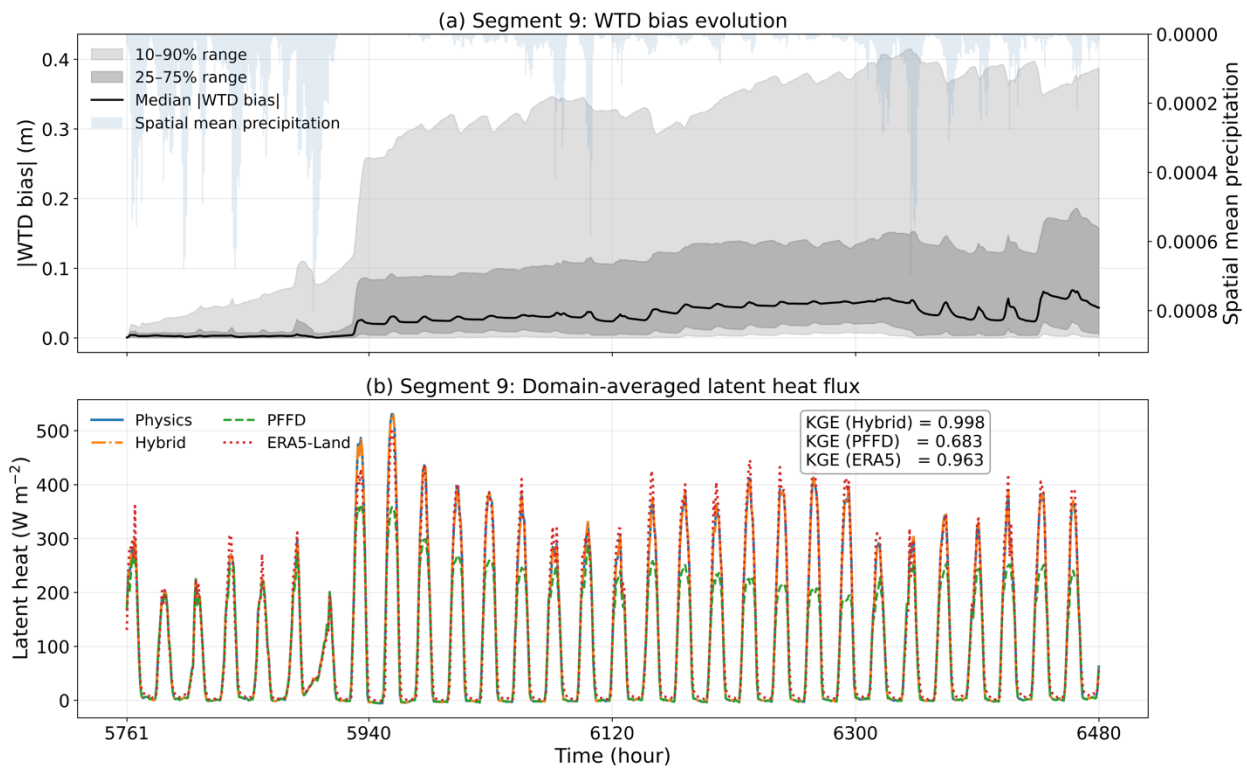
516 Spearman correlation decreases in affected regions, indicating reduced temporal
517 consistency.



518 **Figure 9. Temporal evolution of spatial patterns of near-surface soil moisture and model agreement**
519 **across different prediction stages.** Three periods are shown: early (hours 1–2500), middle (hours 2501–
520 6000), and late (hours 6001–8760) stages of the simulation. For each period, columns represent the
521 physics-based model, the hybrid model, the bias (Hybrid – Physics), and the Spearman correlation
522 coefficient (ρ), respectively.
523

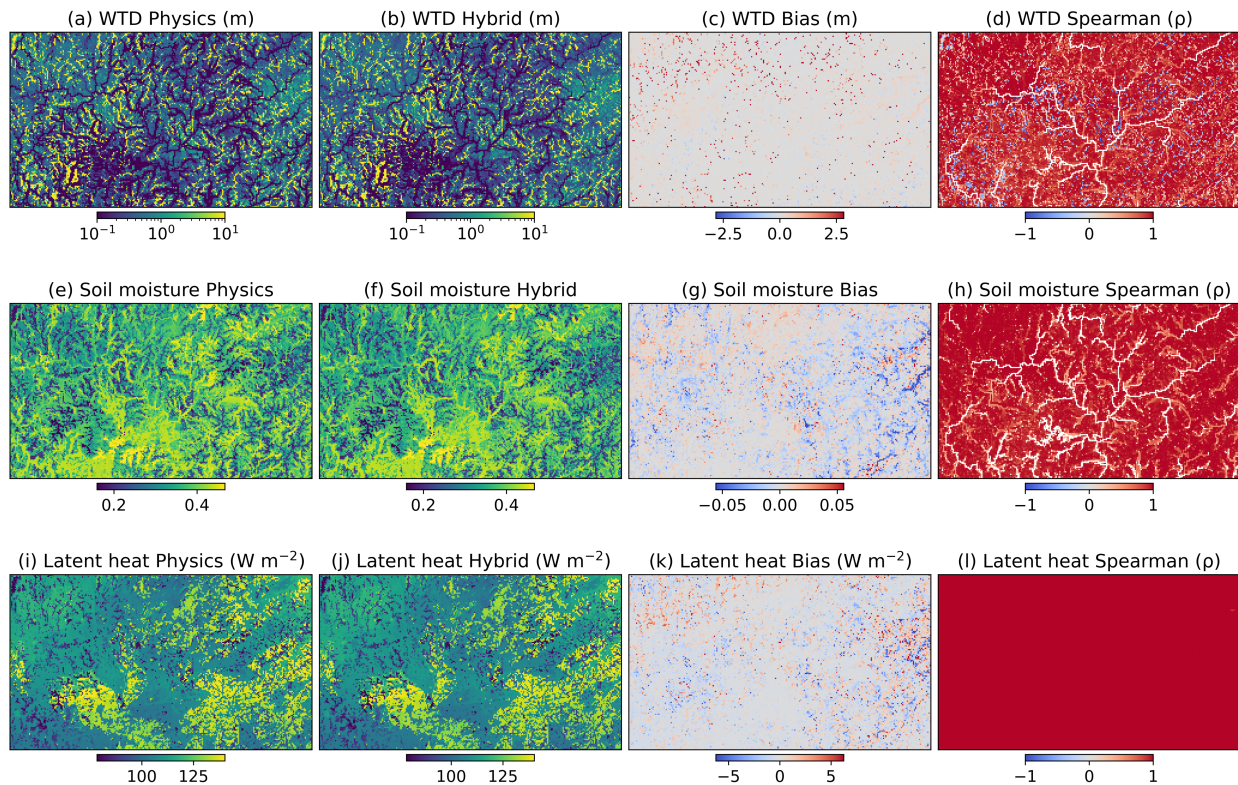
524 This progressive deterioration is closely associated with periods of strong
525 meteorological forcing (e.g., intense precipitation), which amplify discrepancies in
526 groundwater states and accelerate error propagation from subsurface processes to surface
527 variables. Notably, although the overall magnitude of errors may partially decrease during
528 certain periods—as also indicated by the temporal analysis in **Figure 6**—the spatial error
529 structure does not fully recover. This suggests that while the system may exhibit transient
530 stabilization in an aggregated sense, the underlying spatial organization of errors remains
531 altered. These results suggest that the effective prediction horizon of the hybrid system
532 depends on the level of detail required (**Figure 3**): shorter prediction windows are better
533 suited for resolving fine-scale groundwater dynamics, whereas longer simulations can still
534 capture the dominant large-scale feedback patterns despite the loss of spatial detail.

535 To further assess the role of prediction strategy, we divide the full-year simulation into
536 720-hour segments and focus on Segment 9, which exhibits the strongest precipitation
537 variability (**Figure S7**). Despite such strong forcing, the segmented hybrid prediction
538 remains highly consistent with the physics-based simulation (**Figure 10**). In particular, the
539 domain-averaged latent heat flux achieves a KGE of 0.998 relative to the physics-based
540 model, substantially higher than that of the free-drainage configuration (0.683). Compared
541 with the continuous full-year autoregressive simulation, WTD error growth is greatly
542 constrained in this segment. In the full-year run, the median WTD bias increases to about
543 0.3–0.4 m by this stage, with the 25–75% range approaching roughly 0.8–1.0 m and the 10–
544 90% range extending to around 2 m or more. By contrast, under segmented prediction in
545 Segment 9, the median WTD bias remains below about 0.1 m throughout the 720-hour
546 window, the interquartile range is largely confined to about 0.1–0.2 m, and even the 10–90%
547 range stays below about 0.4 m. This indicates that the substantial error amplification seen in
548 the continuous simulation is effectively suppressed when prediction horizons are shortened.



549 **Figure 10. Error evolution and flux consistency during a representative period (Segment 9; hours**
550 **5761–6480).** (a) Temporal evolution of water table depth (WTD) bias in the hybrid model, shown as the
551 median and percentile ranges (25–75% and 10–90%) across the domain, together with spatially averaged
552 precipitation (inverted axis). (b) Domain-averaged latent heat flux from the physics-based model, the
553

554 hybrid model, the free-drainage configuration (PFFD), and the ERA5-Land reanalysis. Kling–Gupta
555 efficiency (KGE) values are computed with respect to the physics-based model.



556 **Figure 11. Spatial performance of the hybrid model under segmented prediction during a high-**
557 **variability period (Segment 9; hours 5761–6480).** The segment corresponds to a period with the largest
558 precipitation variability. Rows show water table depth (WTD), soil moisture, and latent heat, respectively,
559 while columns represent the physics-based model, the hybrid model, the bias (Hybrid – Physics), and the
560 Spearman correlation coefficient (ρ).
561

562 The spatial fields provide equally strong evidence (**Figure 11**). Under segmented
563 prediction, the hybrid model reproduces not only the dominant large-scale organization but
564 also much of the fine-scale structure in WTD, soil moisture, and latent heat. Biases remain
565 spatially scattered rather than coherently organized into large, distorted regions, and
566 Spearman correlation remains uniformly high across most of the domain. This is especially
567 notable in comparison with the late-stage full-year simulation, where fine-scale
568 heterogeneity is strongly degraded and localized regions of reduced agreement become
569 clearly visible.

570 Together, these results indicate that the degradation observed in continuous
571 autoregressive simulations is primarily driven by cumulative error growth, rather than by
572 an intrinsic inability of the hybrid model to represent groundwater–land surface interactions.

573 From an application perspective, a 720-hour (~1 month) prediction window is already
574 sufficient for many flood and drought response scenarios, suggesting that segmented
575 prediction provides a practical balance between computational efficiency and forecast
576 reliability. More broadly, this also implies that future integration with data assimilation
577 could further suppress error drift and extend predictive skill.

578 **4. Conclusions**

579 Three-dimensional groundwater dynamics play a critical role in regulating land-
580 atmosphere interactions through subsurface-surface feedbacks, yet resolving variably
581 saturated flow using the Richards' equation at large scales remains computationally
582 prohibitive. In this study, we developed a hybrid coupling framework that enables the
583 integration of three-dimensional groundwater processes into land surface modeling at
584 substantially reduced computational cost. By replacing the physics-based groundwater
585 solver with a deep learning surrogate while preserving the original coupling interface, the
586 framework provides a practical pathway for incorporating groundwater dynamics into Earth
587 system simulations.

588 The proposed framework was demonstrated in a representative watershed system in the
589 Pearl River Basin, China, where it achieved an approximately 20× computational speedup
590 while retaining the essential interactions between groundwater and land surface processes.
591 Over a full-year hourly simulation, the hybrid system shows strong agreement with the
592 physics-based reference, with a median water table depth (WTD) error within 0.5 m and a
593 domain-averaged latent heat flux KGE of 0.965. Although localized degradation is observed
594 in regions where WTD errors propagate into surface fluxes, the overall spatial and temporal
595 consistency remains robust.

596 Compared to the free-drainage (PFFD) configuration, which represents a conventional
597 land surface modeling approach without explicit groundwater representation, the hybrid
598 framework more effectively captures the influence of groundwater on land surface processes.
599 In addition, segmented simulations at the monthly scale effectively reduce autoregressive
600 error accumulation and maintain stable performance under strong precipitation variability,

601 highlighting the feasibility of multi-timescale, on-demand simulation strategies within this
602 framework.

603 Overall, this study demonstrates the feasibility of a hybrid surrogate–physics coupling
604 approach for representing three-dimensional groundwater dynamics in land surface
605 modeling. The framework provides a flexible foundation for future extensions, including
606 applications across diverse hydroclimatic conditions, as well as integration with data
607 assimilation and Earth system modeling frameworks.

608 **Code and data availability**

609 The CoLM/ParFlow model used in this study to generate the datasets is available at
610 <https://doi.org/10.5281/zenodo.16879407> (Yang, 2025a), with a copy also provided on
611 GitHub at <https://github.com/aureliayang/parflow-cola>. The hybrid model developed in
612 this study is available at <https://doi.org/10.5281/zenodo.17412339> (Yang, 2025b), with its
613 source code maintained on GitHub at <https://github.com/aureliayang/ParFlow-nn>.

614 **Acknowledgements**

615 This research was supported by the National Natural Science Fund for Excellent Young
616 Scientists (Overseas) (grant no. 24EAA00330), the Fundamental Research Funds for the
617 Central Universities – Young Faculty Development Program (grant no. 25hytd008), the
618 National High-Level Young Talent Program (Provincial Government Matching Research
619 Funds) (grant no. 2025HYSPT0705), and the Guangdong Major Project of Basic and Applied
620 Basic Research (grant no. 2021B0301030007).

621 **Competing interests**

622 The contact author has declared that none of the authors has any competing interests.

623 **References**

- 624 Bennett, A., Tran, H., De la Fuente, L., Triplett, A., Ma, Y., Melchior, P., Maxwell, R. M., &
625 Condon, L. E. (2024). Spatio-Temporal Machine Learning for Regional to Continental
626 Scale Terrestrial Hydrology. *Journal of Advances in Modeling Earth Systems*, 16(6),
627 e2023MS004095. <https://doi.org/https://doi.org/10.1029/2023MS004095>
- 628 Chapman, W. E., & Berner, J. (2025). Improving Climate Bias and Variability via CNN-Based
629 State-Dependent Model-Error Corrections. *Geophysical Research Letters*, 52(6),
630 e2024GL114106. <https://doi.org/https://doi.org/10.1029/2024GL114106>
- 631 Chen, M., Qian, Z., Boers, N., Jakeman, A. J., Kettner, A. J., Brandt, M., Kwan, M.-P., Batty, M.,
632 Li, W., Zhu, R., Luo, W., Ames, D. P., Barton, C. M., Cuddy, S. M., Koirala, S., Zhang, F.,
633 Ratti, C., Liu, J., Zhong, T.,...Lü, G. (2023). Iterative integration of deep learning in hybrid
634 Earth surface system modelling. *Nature Reviews Earth & Environment*, 4(8), 568-581.
635 <https://doi.org/10.1038/s43017-023-00452-7>
- 636 Chen, S., Li, L., Wei, Z., Wei, N., Zhang, Y., Zhang, S., Yuan, H., Shangguan, W., Zhang, S., Li,
637 Q., & Dai, Y. (2024). Exploring Topography Downscaling Methods for Hyper-Resolution
638 Land Surface Modeling. *Journal of Geophysical Research: Atmospheres*, 129(20),
639 e2024JD041338. <https://doi.org/https://doi.org/10.1029/2024JD041338>

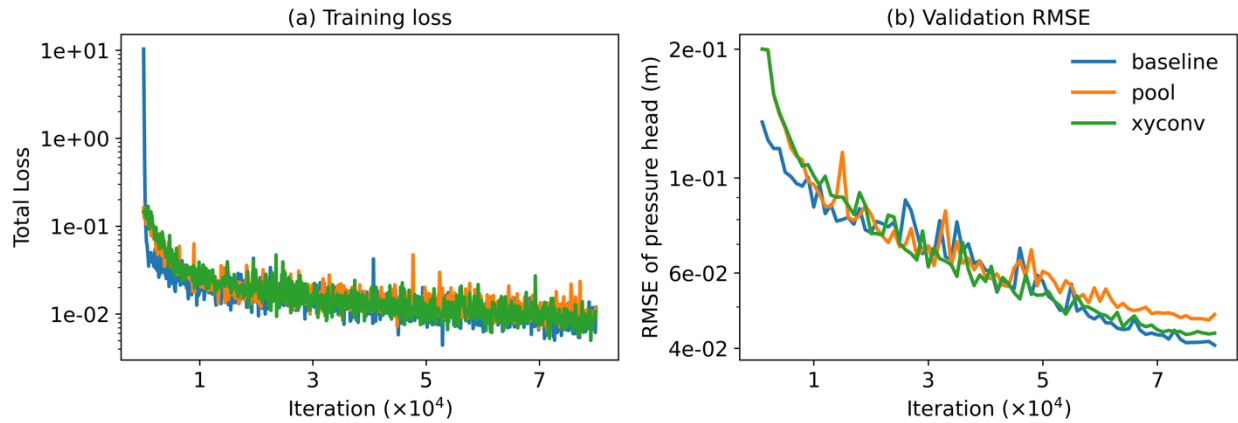
- 640 Christopoulos, C., Lopez-Gomez, I., Beucler, T., Cohen, Y., Kawczynski, C., Dunbar, O. R. A., &
641 Schneider, T. (2024). Online Learning of Entrainment Closures in a Hybrid Machine
642 Learning Parameterization. *Journal of Advances in Modeling Earth Systems*, 16(11),
643 e2024MS004485. <https://doi.org/https://doi.org/10.1029/2024MS004485>
- 644 Clark, S. K., Watt-Meyer, O., Kwa, A., McGibbon, J., Henn, B., Perkins, W. A., Wu, E., Bretherton,
645 C. S., & Harris, L. M. (2024). ACE2-SOM: Coupling to a slab ocean and learning the
646 sensitivity of climate to changes in CO₂. *arXiv e-prints*, arXiv: 2412.04418.
- 647 Cremer, C. J. M., Mariegaard, J. S., & Andersson, H. J. (2025). A hybrid data assimilation and
648 machine learning approach for enhancing operational forecasting in 2D hydrodynamic
649 models. *Journal of Hydroinformatics*, 27(3), 493-507.
650 <https://doi.org/10.2166/hydro.2025.289>
- 651 Cresswell-Clay, N., Liu, B., Durran, D. R., Liu, Z., Espinosa, Z. I., Moreno, R. A., & Karlbauer,
652 M. (2025). A Deep Learning Earth System Model for Efficient Simulation of the Observed
653 Climate. *AGU Advances*, 6(4), e2025AV001706.
654 <https://doi.org/https://doi.org/10.1029/2025AV001706>
- 655 Dai, T., Maher, K., & Perzan, Z. (2025). Machine learning surrogates for efficient hydrologic
656 modeling: Insights from stochastic simulations of managed aquifer recharge. *Journal of*
657 *Hydrology*, 652, 132606. <https://doi.org/https://doi.org/10.1016/j.jhydrol.2024.132606>
- 658 Duncan, J. P., Wu, E., Dheeshjith, S., Subel, A., Arcomano, T., Clark, S. K., Henn, B., Kwa, A.,
659 McGibbon, J., & Perkins, W. A. (2025). SamudrACE: Fast and Accurate Coupled Climate
660 Modeling with 3D Ocean and Atmosphere Emulators. *arXiv preprint arXiv:2509.12490*.
- 661 Eilander, D., van Verseveld, W., Yamazaki, D., Weerts, A., Winsemius, H. C., & Ward, P. J. (2021).
662 A hydrography upscaling method for scale-invariant parametrization of distributed
663 hydrological models. *Hydrol. Earth Syst. Sci.*, 25(9), 5287-5313.
664 <https://doi.org/10.5194/hess-25-5287-2021>
- 665 Fan, Y., Miguez-Macho, G., Weaver, C. P., Walko, R., & Robock, A. (2007). Incorporating water
666 table dynamics in climate modeling: 1. Water table observations and equilibrium water
667 table simulations. *Journal of Geophysical Research: Atmospheres*, 112(D10).
668 <https://doi.org/https://doi.org/10.1029/2006JD008111>
- 669 Friedl, M., & Sulla-Menashe, D. (2022). Modis/terra+ aqua land cover type yearly 13 global 500m
670 sin grid v061. NASA EOSDIS Land Processes Distributed Active Archive Center. DOI:
671 https://doi.org/10.5067/MODIS/MCD12Q1_61.
- 672 Gleeson, T., Smith, L., Moosdorf, N., Hartmann, J., Durr, H. H., Manning, A. H., van Beek, L. P.
673 H., & Jellinek, A. M. (2011). Mapping permeability over the surface of the Earth.
674 *Geophysical Research Letters*, 38. <https://doi.org/Artn L0240110.1029/2010gl045565>
- 675 Kollet, S. J., & Maxwell, R. M. (2008). Capturing the influence of groundwater dynamics on land
676 surface processes using an integrated, distributed watershed model. *Water Resources*
677 *Research*, 44(2). <https://doi.org/Artn W0240210.1029/2007wr006004>
- 678 Lim, B., Arik, S. Ö., Loeff, N., & Pfister, T. (2021). Temporal Fusion Transformers for
679 interpretable multi-horizon time series forecasting. *International Journal of Forecasting*,
680 37(4), 1748-1764. <https://doi.org/https://doi.org/10.1016/j.ijforecast.2021.03.012>
- 681 Lin, J., Yu, S., Peng, L., Beucler, T., Wong-Toi, E., Hu, Z., Gentine, P., Geleta, M., & Pritchard, M.
682 (2023). Sampling hybrid climate simulation at scale to reliably improve machine learning
683 parameterization. *arXiv preprint arXiv:2309.16177*.
- 684 Liu, H.-Y., Satoh, M., Gu, J.-F., Lei, L., Tang, J., Tan, Z.-M., Wang, Y., & Xu, J. (2023).
685 Predictability of the Most Long-Lived Tropical Cyclone Freddy (2023) During Its

- 686 Westward Journey Through the Southern Tropical Indian Ocean. *Geophysical Research*
687 *Letters*, 50(20), e2023GL105729. <https://doi.org/https://doi.org/10.1029/2023GL105729>
- 688 Liu, H.-Y., Tan, Z.-M., Wang, Y., Tang, J., Satoh, M., Lei, L., Gu, J.-F., Zhang, Y., Nie, G.-Z., &
689 Chen, Q.-Z. (2024). A Hybrid Machine Learning/Physics-Based Modeling Framework for
690 2-Week Extended Prediction of Tropical Cyclones. *Journal of Geophysical Research:*
691 *Machine Learning and Computation*, 1(3), e2024JH000207.
692 <https://doi.org/https://doi.org/10.1029/2024JH000207>
- 693 Liu, Y., Huang, H., Wang, S. C., Zhang, T., Xu, D., & Chen, Y. (2025). ELM2.1-XGBfire1.0:
694 improving wildfire prediction by integrating a machine learning fire model in a land surface
695 model. *Geosci. Model Dev.*, 18(13), 4103-4117. [https://doi.org/10.5194/gmd-18-4103-](https://doi.org/10.5194/gmd-18-4103-2025)
696 [2025](https://doi.org/10.5194/gmd-18-4103-2025)
- 697 Maxwell, R. M., Condon, L. E., & Melchior, P. (2021). A Physics-Informed, Machine Learning
698 Emulator of a 2D Surface Water Model: What Temporal Networks and Simulation-Based
699 Inference Can Help Us Learn about Hydrologic Processes. *Water*, 13(24), 3633.
700 <https://www.mdpi.com/2073-4441/13/24/3633>
- 701 Maxwell, R. M., & Miller, N. L. (2005). Development of a coupled land surface and groundwater
702 model. *Journal of Hydrometeorology*, 6(3), 233-247. <https://doi.org/10.1175/JHM2332>
703 [ISI>://WOS:000230393600001](https://doi.org/10.1175/JHM2332)
- 704 Muñoz-Sabater, J., Dutra, E., Agustí-Panareda, A., Albergel, C., Arduini, G., Balsamo, G.,
705 Boussetta, S., Choulga, M., Harrigan, S., Hersbach, H., Martens, B., Miralles, D. G., Piles,
706 M., Rodríguez-Fernández, N. J., Zsoter, E., Buontempo, C., & Thépaut, J. N. (2021).
707 ERA5-Land: a state-of-the-art global reanalysis dataset for land applications. *Earth Syst.*
708 *Sci. Data*, 13(9), 4349-4383. <https://doi.org/10.5194/essd-13-4349-2021>
- 709 Niu, Z., Wang, D., Mu, M., Huang, W., Fan, X., Yang, M., & Qin, B. (2025). Machine-Learning
710 (ML)-Physics Fusion Model Accelerates the Paradigm Shift in Typhoon Forecasting With
711 a CNOP-Based Assimilation Framework. *Geophysical Research Letters*, 52(15),
712 e2025GL115926. <https://doi.org/https://doi.org/10.1029/2025GL115926>
- 713 Shangguan, W., Dai, Y., Duan, Q., Liu, B., & Yuan, H. (2014). A global soil data set for earth
714 system modeling. *Journal of Advances in Modeling Earth Systems*, 6(1), 249-263.
715 <https://doi.org/10.1002/2013ms000293>
- 716 Tran, H., Leonarduzzi, E., De la Fuente, L., Hull, R. B., Bansal, V., Chennault, C., Gentine, P.,
717 Melchior, P., Condon, L. E., & Maxwell, R. M. (2021). Development of a Deep Learning
718 Emulator for a Distributed Groundwater–Surface Water Model: ParFlow-ML.
719 *Water*, 13(23), 3393. <https://www.mdpi.com/2073-4441/13/23/3393>
- 720 van Genuchten, M. T. (1980). A Closed-form Equation for Predicting the Hydraulic Conductivity
721 of Unsaturated Soils. *Soil Science Society of America Journal*, 44(5), 892-898.
722 <https://doi.org/https://doi.org/10.2136/sssaj1980.03615995004400050002x>
- 723 Wang, Y., Wu, H., Zhang, J., Gao, Z., Wang, J., Philip, S. Y., & Long, M. (2022). Predrnn: A
724 recurrent neural network for spatiotemporal predictive learning. *IEEE Transactions on*
725 *Pattern Analysis and Machine Intelligence*, 45(2), 2208-2225.
- 726 Watt-Meyer, O., Dresdner, G., McGibbon, J., Clark, S. K., Henn, B., Duncan, J., Brenowitz, N. D.,
727 Kashinath, K., Pritchard, M. S., & Bonev, B. (2023). ACE: A fast, skillful learned global
728 atmospheric model for climate prediction. *arXiv preprint arXiv:2310.02074*.
- 729 Xiong, Z., Zhang, Z., Gui, H., Zhu, P., Sun, Y., Zhou, X., Xiao, K., & Xin, Q. (2024). Predicting
730 time series of vegetation leaf area index across North America based on climate variables

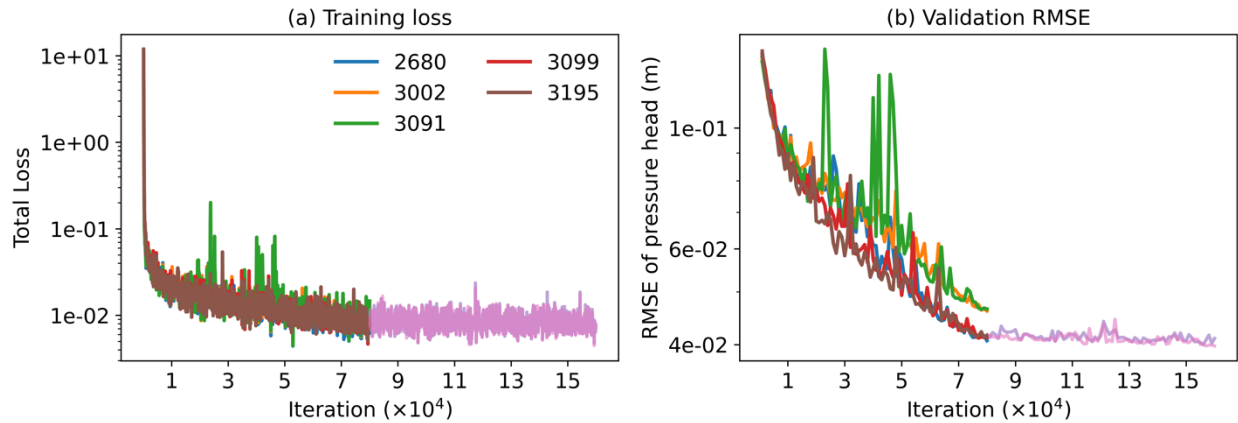
- 731 for land surface modeling using attention-enhanced LSTM. *International Journal of*
732 *Digital Earth*, 17(1), 2372317. <https://doi.org/10.1080/17538947.2024.2372317>
- 733 Yang, C. (2025a). ParFlow-CoLM [code]. *Zenodo*.
734 <https://doi.org/10.5281/zenodo.16879407>
- 735 Yang, C. (2025b). ParFlow and CoLM physics-ML hybrid coupling [code]. *Zenodo*.
736 <https://doi.org/10.5281/zenodo.17412339>
- 737 Yang, C., Jia, Z., Xu, W., Wei, Z., Zhang, X., Zou, Y., McDonnell, J., Condon, L., Dai, Y., &
738 Maxwell, R. (2025). CONCN: a high-resolution, integrated surface water–groundwater
739 ParFlow modeling platform of continental China. *Hydrol. Earth Syst. Sci.*, 29(9), 2201-
740 2218. <https://doi.org/10.5194/hess-29-2201-2025>
- 741 Yang, C., Li, H.-Y., Fang, Y., Cui, C., Wang, T., Zheng, C., Leung, L. R., Maxwell, R. M., Zhang,
742 Y.-K., & Yang, X. (2020). Effects of Groundwater Pumping on Ground Surface
743 Temperature: A Regional Modeling Study in the North China Plain. *Journal of Geophysical*
744 *Research: Atmospheres*, 125(9), e2019JD031764. <https://doi.org/10.1029/2019jd031764>
- 745 Yang, C., Sun, A., Zhang, S., Dai, Y., Kollet, S., & Maxwell, R. (2026). 20 years of trials and
746 insights: bridging legacy and next generation in ParFlow and Land Surface Model
747 Coupling. *Geosci. Model Dev.*, 19(5), 1849-1866. [https://doi.org/10.5194/gmd-19-1849-](https://doi.org/10.5194/gmd-19-1849-2026)
748 [2026](https://doi.org/10.5194/gmd-19-1849-2026)
- 749 Yang, Y., Feng, D., Beck, H. E., Hu, W., Abbas, A., Sengupta, A., Delle Monache, L., Hartman, R.,
750 Lin, P., Shen, C., & Pan, M. (2025). Global Daily Discharge Estimation Based on Grid
751 Long Short-Term Memory (LSTM) Model and River Routing. *Water Resources Research*,
752 61(6), e2024WR039764. <https://doi.org/https://doi.org/10.1029/2024WR039764>
- 753 Yu, S., Hannah, W., Peng, L., Lin, J., Bhouri, M. A., Gupta, R., Lütjens, B., Will, J. C., Behrens,
754 G., & Busecke, J. (2023). ClimSim: A large multi-scale dataset for hybrid physics-ML
755 climate emulation. *Advances in neural information processing systems*, 36, 22070-22084.
- 756 Yu, S., Hu, Z., Subramaniam, A., Hannah, W., Peng, L., Lin, J., Bhouri, M. A., Gupta, R., Lütjens,
757 B., & Will, J. C. (2025). ClimSim-Online: A Large Multi-Scale Dataset and Framework for
758 Hybrid Physics-ML Climate Emulation. *Journal of Machine Learning Research*, 26(142),
759 1-85.
- 760 Yuan, H., & Dai, Y. (2025). *Description of the Common Land Model (CoLM 2024)*. Sun Yat-sen
761 University Press.
- 762 Zheng, H., Lin, F., Feng, X., & Chen, Y. (2021). A Hybrid Deep Learning Model With Attention-
763 Based Conv-LSTM Networks for Short-Term Traffic Flow Prediction. *IEEE Transactions*
764 *on Intelligent Transportation Systems*, 22(11), 6910-6920.
765 <https://doi.org/10.1109/TITS.2020.2997352>

766
767
768

769 **Supplementary Information**



770
771 **Figure S1.** Training loss and validation RMSE of the ParFlow surrogate model for different
772 architectural configurations. (a) Evolution of the training loss. (b) Validation RMSE of
773 pressure head. The baseline model and variants with alternative spatial aggregation
774 strategies (pooling and xyconv) exhibit similar convergence behavior and comparable
775 validation performance.
776

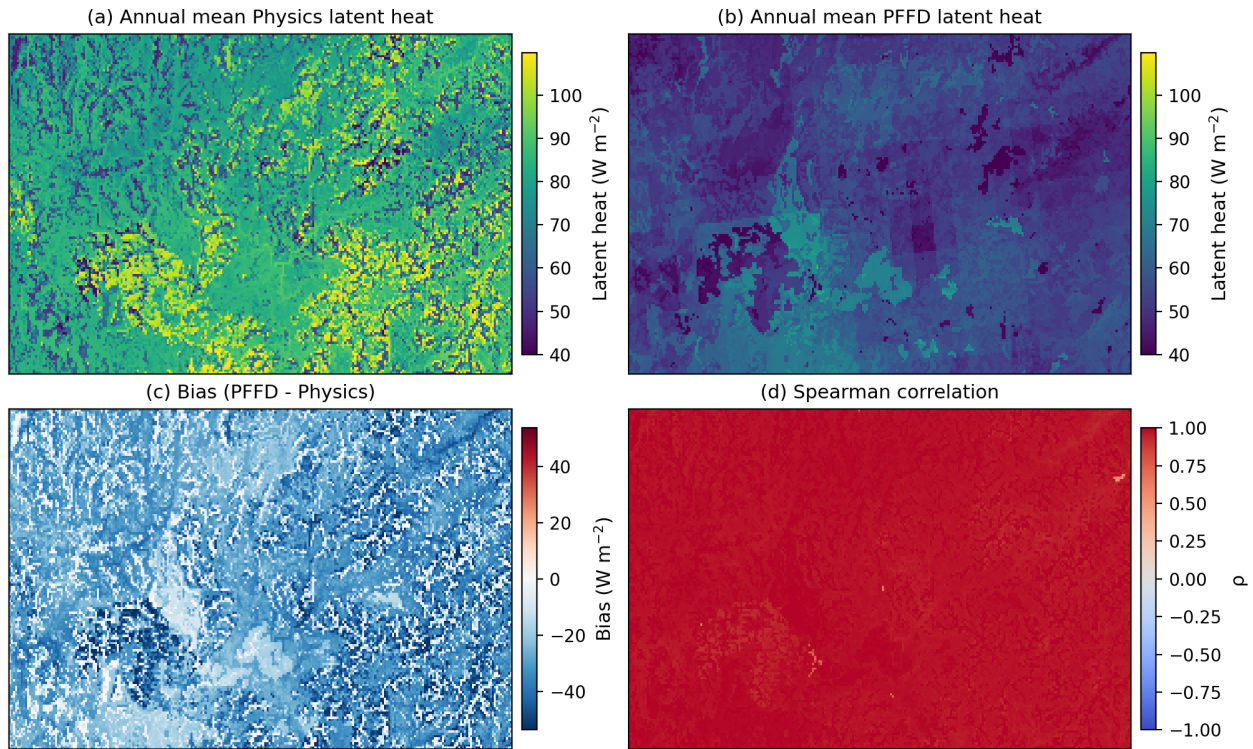


777
778 **Figure S2.** Training loss and validation performance across repeated training runs of the
779 ParFlow surrogate model. (a) Evolution of the training loss during optimization. (b)
780 Validation RMSE of pressure head over training iterations.
781
782
783



784
785
786
787

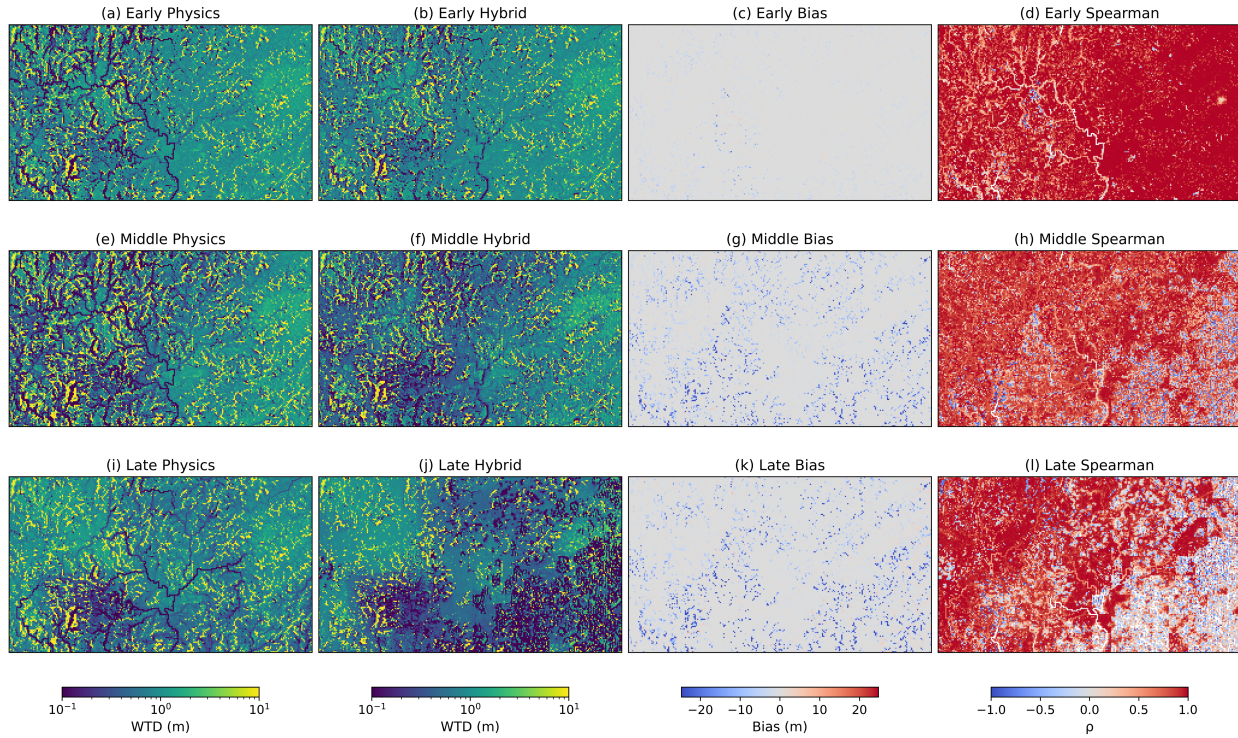
Figure S3. Spatial distributions of land cover and soil texture in the study domain. (a) Land cover classification. (b) Soil texture classes.



788

789 **Figure S4. Spatial comparison of annual mean latent heat flux and model agreement**
790 **between the physics-based and free-drainage (PFFD) configurations.** (a) Annual mean
791 latent heat flux from the physics-based model. (b) Annual mean latent heat flux from the
792 PFFD configuration. (c) Bias (PFFD – Physics). (d) Spearman rank correlation coefficient (ρ)
793 computed from the temporal series at each grid cell.

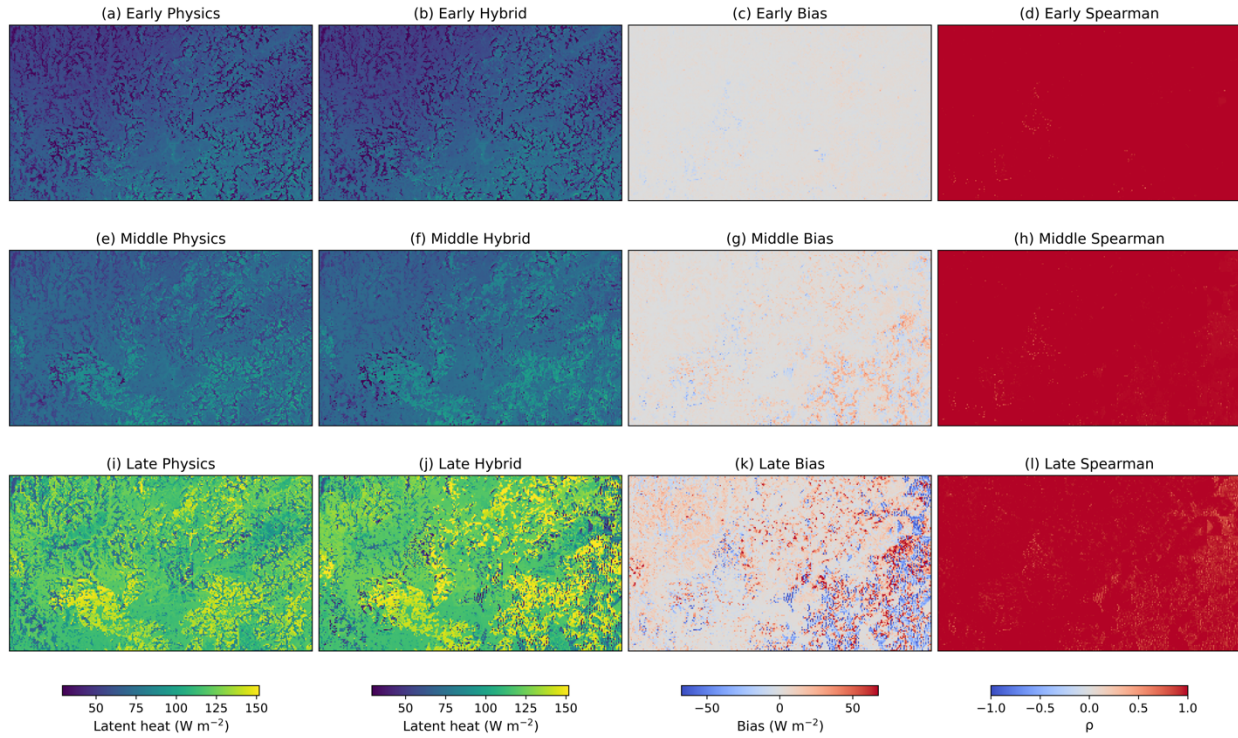
794



795

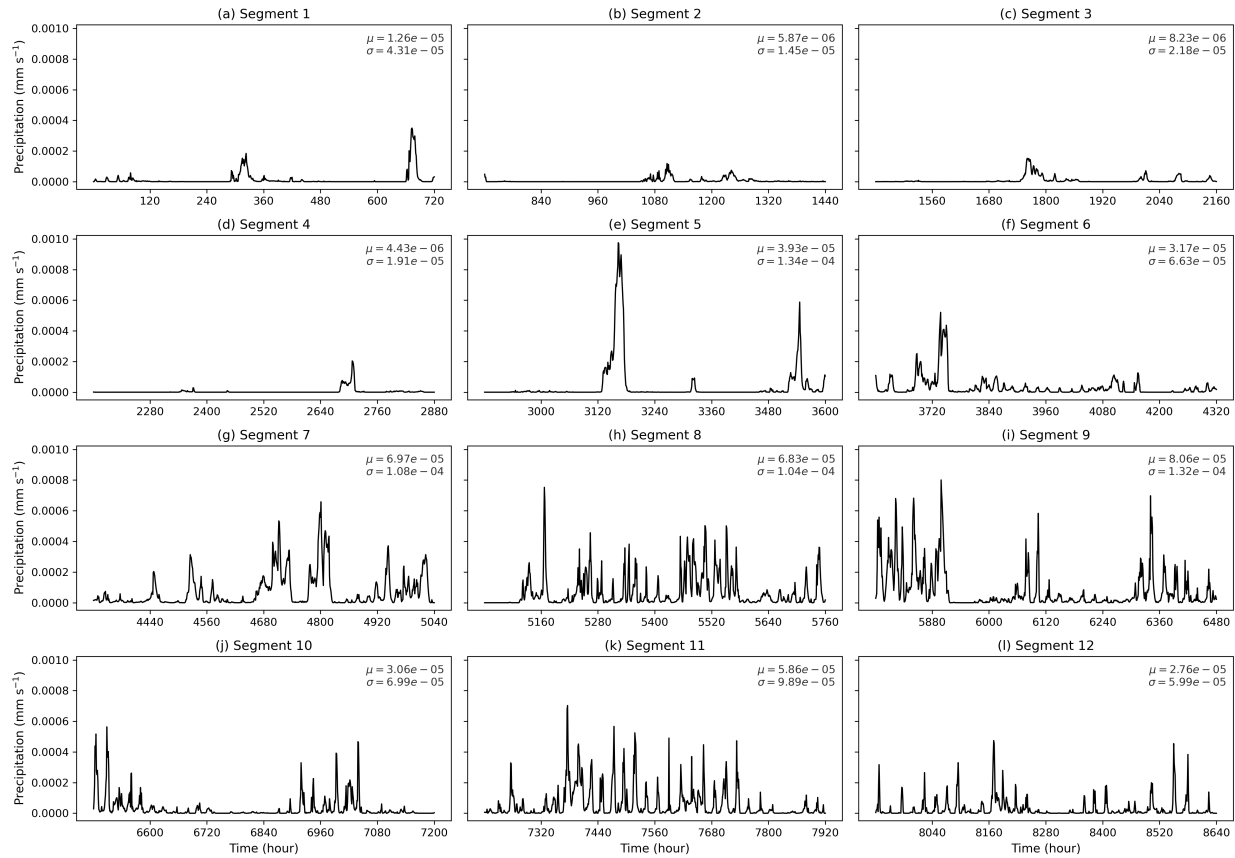
796 **Figure S5. Temporal evolution of spatial patterns of water table depth (WTD) and model**
797 **agreement across different prediction stages.** Three periods are shown: early (hours 1–
798 2500), middle (hours 2501–6000), and late (hours 6001–8760) stages of the simulation. For
799 each period, columns represent the physics-based model, the hybrid model, the bias (Hybrid
800 – Physics), and the Spearman correlation coefficient (ρ), respectively.

801



802

803 **Figure S6. Temporal evolution of spatial patterns of latent heat flux and model agreement**
804 **across different prediction stages.** Three periods are shown: early (hours 1–2500), middle
805 (hours 2501–6000), and late (hours 6001–8760) stages of the simulation. For each period,
806 columns represent the physics-based model, the hybrid model, the bias (Hybrid – Physics),
807 and the Spearman correlation coefficient (ρ), respectively.



808
809 **Figure S7. Segmented time series of precipitation over the simulation period (WY2021).**
810 The full-year hourly precipitation is divided into 12 consecutive segments (a-l), each
811 spanning an equal duration. For each segment, the temporal variability is illustrated, and the
812 mean (μ) and standard deviation (σ) are annotated to quantify differences in precipitation
813 intensity and variability across periods. The segmentation highlights the intermittent and
814 highly heterogeneous nature of precipitation, with distinct periods of low activity and
815 intense events.

816
817
818